JOURNAL OF GEOPHYSICAL RESEARCH, VOL. ???, XXXX, DOI:10.1029/,

Understanding the Variability of Nightside Temperatures, NO UV and O_2 IR Nightglow Emissions in the Venus Upper Atmosphere

A. S. Brecht[1], S. W. Bougher[1], J. -C. Gérard[2], C. D. Parkinson[1], S. Rafkin[3], B. Foster[4]

[1]Department of Atmospheric, Oceanic, and Space Sciences, University of Michigan, Ann Arbor, MI, USA.

[2]Laboratoire de Physique Atmosphérique et Planétaire, Université de Liège, Liège, Belgium.

[3]Department of Space Studies, Southwest Research Institute, Boulder, Colorado, USA.

[4]High Altitude Observatory, National Center for Atmospheric Research, Boulder, Colorado, USA.

Abstract.

Venus Express (VEx) has been monitoring key nightglow emissions and thermal features (O_2 IR nightglow, NO UV nightglow, and nightside temperatures) which contribute to a comprehensive understanding of the global dynamics and circulation patterns above ∼90 km. The nightglow emissions serve as effective tracers of Venus' middle and upper atmosphere global wind system due to their variable peak brightness and horizontal distributions. A statistical map has been created utilizing O_2 IR nightglow VEx observations and a statistical map for NO UV is being developed. A nightside warm layer near 100 km has been observed by VEx and ground based observations. The National Center for Atmospheric Research (NCAR) Venus Thermospheric General Circulation Model (VTGCM) has been updated and revised in order to address these key VEx observations and provide diagnostic interpretation. The VTGCM is first used to capture the statistically averaged mean state of these three key observations. This correspondence implies a weak retrograde superrotating zonal flow (RSZ) from ∼80 km to 110 km and above 110 km the emergence of modest RSZ winds approaching 60 m s^{-1} above ∼130 km. Subsequently, VTGCM sensitivity tests are performed using two tuneable parameters (the nightside eddy diffusion coefficient and the wave drag term) to examine corresponding variability within the VTGCM. These tests identified a possible mechanism for the observed non-correlation of the O_2 and NO emissions. The dynamical explanation

requires the nightglow layers to be at least $\sim$15 km apart and the retrograde zonal wind to increase dramatically over 110 to 130 km.

1. Introduction

After the Pioneer Venus Orbiter (PVO) mission ended in 1992 and the Magellan mission in 1994, fundamental questions still remained about our neighboring planet Venus. Currently, Venus Express (VEx) is orbiting Venus with a goal to address many of these fundamental questions and to provide a detailed study of Venus' atmosphere. This paper discusses Venus' unique global circulation and the processes that drive the variability in the upper atmosphere. Specifically, this study focuses on nightglow, a diagnostic used for understanding the upper atmosphere dynamics and global circulation. The intensity and distribution of nightglow emissions provide information about the circulation (strength of winds and altitude variations). Nightglow emissions can be observed from Earth and spacecraft, consequently providing a proxy for the day to night flow. We will approach this question numerically with a three-dimensional (3-D) model and compare the model results to several VEx data sets.

From past observations it has been noted that Venus' upper atmosphere has two dominating circulation patterns (see Figure 1) [e.g. *Bougher et al.*, 1997, 2006; *Lellouch et al.*, 1997; *Schubert et al.*, 2007]. One pattern occurs in the region between the surface of the planet to the top of the cloud deck at $\sim$70 km. This region is dominated by a wind pattern flowing in the direction of the planets spin and is faster than Venus' rotation. This flow is known as a retrograde superrotating zonal flow (RSZ). The second pattern occurs above $\sim$120 km and is a relatively stable mean subsolar-to-antisolar flow (SS-AS) [*Bougher et al.*, 1997]. In the upper atmosphere, Venus has inhomogeneous heating by solar radiation (EUV, UV, and IR) thus providing large pressure gradients to generate the dominant SS-AS flow pattern [*Dickinson and Ridley*, 1977; *Schubert et al.*, 1980; *Bougher et al.*, 1997]. In the altitude range of 70-120 km, also known as

the transition region, the two major flow patterns are presumed to be superimposed; meaning both flows can be dominant in this altitude region while below this region RSZ is dominate with little evidence of a SS-AS flow and above this region SS-AS is dominate with a minor RSZ flow. Observations suggest a high degree of variability of these wind components in the transition region.

This interaction produces at least three modifications to the general flow in the upper atmosphere: (a) a shift in the divergence of the flow from the subsolar point toward the morning terminator, (b) stronger evening terminator winds than those along the morning terminator, and (c) a shift in the convergence of the flow away from midnight and toward the morning terminator [*Schubert et al.*, 2007]. These modifications also vary with altitude which reflects the changing importance of underlying drivers and solar cycle variations. The specific processes responsible for maintaining and driving variations in the SS-AS and RSZ wind components in Venus' upper atmosphere are still not well understood or quantified. More importantly, the interaction between the two flows occurs in a region where there is limited spacecraft and ground based data and for which modeling is most challenging.

1.1. Pre VEx Datasets

These characteristics of Venus' upper atmosphere dynamics have been gleaned from a number of remote and in-situ datasets collected at the planet. A thorough examination of PVO neutral density (e.g., CO_2, O, He, and H) and temperature distributions above $\sim$130 km has been used to constrain general circulation model simulations, from which SS-AS and RSZ wind magnitudes can be extracted (see reviews by *Bougher et al.* [1997] and see table 1 in *Bougher et al.* [2006]). The spatial distribution of PVO ultraviolet (UV) night airglow emissions (e.g. NO), PVO UV dayglow emissions (e.g. atomic O), and H-Lyman-α emissions, have all been used to trace

the circulation patterns at thermospheric altitudes above ∼115 km. Visible and infrared (IR) O_2 nightglow distributions from Veneras 9 and 10, Galileo, PVO and the ground, along with minor species distributions (especially CO) have also been used to constrain upper mesospheric wind patterns (∼80-110 km) [see review by *Lellouch et al.*, 1997]. Many of these datasets are discussed in detail in *Bougher et al.* [1997], *Lellouch et al.* [1997], and *Schubert et al.* [2007]. See a summary in *Bougher et al.* [2006] table 1 for more detailed information.

Connes et al. [1979] were the first to observe O_2 IR night airglow at 1.27 μm by using a ground-based Fourier transform spectrometer. Recent ground-based observations have been performed by *Crisp et al.* [1996]; *Ohtsuki et al.* [2005, 2008]; *Bailey et al.* [2008]. *Crisp et al.* [1996] documented, from 1990 to 1994, the O_2 nightglow peak emission ranging from 0.5 MR to 6 MR (MR = Mega-Rayleigh = 10^{12} photons $cm^{-2}s^{-1}$ into 4π sr) with a nightside-averaged emission rate near 1 MR. The bright regions varied spatially and temporally, but on average occurred in lower latitudes between local times of 00:00 and 03:00. The nightglow observations yielded a rotational temperature of 186±6 K in the altitude range of 90 - 115 km. *Ohtsuki et al.* [2005, 2008] had three different observation periods (2002, 2004, 2005) and observed peak emissions from 1-3 MR with the bright region near the anti-solar point but varied day-to-day. Their average rotational temperatures from these nightglow observations were 193±9 K, 182±25 K, and 185±20 K, which also showed an association with the nightglow patches of the peak emission. *Bailey et al.* [2008] observed during two different time sequences in 2004 and 2005 and discerned the peak emission to range from 1.5-4.8 MR with the bright region occurring in low latitudes around the anti-solar point but occasionally had a displacement of ∼2 hours toward the morning terminator. They derived temperatures from 181 to 196 K and also showed the connection of warmer temperatures with the nightglow patches. From these

few ground observations, a basic understanding of the dynamics in the upper mesosphere/lower thermosphere region where the O_2 nightglow occurs was developed.

The NO UV night airglow provides information higher in the atmosphere. The NO UV nightglow peak layer is observed in a range from ∼95-132 km. The NO UV nightglow consists of δ (190-240 nm) and γ (225-270 nm) bands and was observed first by two different groups; *Feldman et al.* [1979] and *Stewart and Barth* [1979]. *Feldman et al.* [1979] detected the nightglow with the ultraviolet spectrograph on the International Ultraviolet Explorer (IUE), while *Stewart and Barth* [1979] used the ultraviolet spectrometer on PVO. *Stewart et al.* [1980] provided images only for the strongest δ (0,1) band from Pioneer Venus. The observations suggested large day-to-day variations and the peak emission regions varied in intensity and location. *Stewart et al.* [1980] stated that, on average, the nightglow peak for the δ (0,1) band was located near 02:00 local time (LT) and slightly south of the equator. The average peak emission rate for the bright region, after revision by *Bougher et al.* [1990], was determined to be ∼1.9 kR (kR = kilo-Rayleigh) for the δ (0,1) band. *Gérard et al.* [1981] determined the altitude of the peak emission to be near 115 ± 2 km from PVO limb observations near periapsis. The NO UV and O_2 IR nightglows are consistently observed in the transition region of the Venus upper atmosphere. Other observations from VEx will be discussed in section 1.2.

In addition, PVO made a surprising discovery about Venus' thermospheric temperatures. Temperatures on the dayside at 100 km are ∼180 K and increase to ∼300 K at the exobase; on the nightside temperatures are ∼180 K at 100 km and decrease to ∼100 - 120 K at the exobase [*Schubert et al.*, 1980; *Bougher et al.*, 1997]. This unusual nightside upper atmosphere region (>100 km) has been designated as the Venus "cryosphere" [*Keating et al.*, 1979; *Schu-*

bert et al., 1980]. The reasons for the existence of the cryosphere have been examined using hydrodynamic models [*Bougher et al.*, 2006; *Schubert et al.*, 2007].

Venus' rotation is very slow with its day being longer than its year, giving rise to large day-night pressure gradients and very strong SS-AS winds. By using nominal input parameters, the upper atmospheric winds were simulated yielding higher flow speeds than inferred from these datasets (spacecraft and ground based). These simulations produced much too warm nightside temperatures due to compressional heating [*Dickinson and Ridley*, 1977; *Schubert et al.*, 1980]. Thus there is evidence of a decelerating mechanism needed to model the winds appropriately [e.g. *Alexander*, 1992; *Zhang et al.*, 1996; *Bougher et al.*, 1997]. Understanding how the atmosphere is decelerated is important since the net day-to-night upper atmosphere circulation, above 90 km, produces nightside downwelling and is crucial for maintaining the observed cold nightside temperatures ($\sim$100 - 120 K) and the measured density structure. The deceleration mechanism is likely not symmetric in local time, since the net zonal winds appear stronger at the evening terminator then the morning terminator [*Bougher et al.*, 1997].

Lastly, ground-based wind measurements have been made using several different techniques; CO_2 10-μm infrared heterodyne spectroscopy, CO millimeter and sub-millimeter measurements, CO emission lines at 4.7 μm, and visible observations of reflected solar lines. For brevity, only a few observations will be discussed and the reader is referred to table 1 in *Lellouch et al.* [1997] and table 1 in *Bougher et al.* [2006] for more details.

Goldstein et al. [1991] observed (December 1985 and March 1987) absolute wind velocities near 110$\pm$10 km altitude using the CO_2 10-μm infrared heterodyne spectroscopy technique. The observations provided a SS-AS circulation near 120$\pm$30 m s^{-1} along with a small superimposed RSZ wind component of 25$\pm$15 m s^{-1}. At slightly lower altitudes ($\sim$99 km) CO

J(0-1) millimeter measurements were made during late April and early May 1988 by *Shah et al.* [1991]. At these times, strong RSZ wind speeds of $\sim$130$\pm$10 m s^{-1} were dominant, while the SS-AS wind was very small. Other observations have been made, specifically by the CO lines at 4.7 μm which calculated a total wind (zonal wind + 0.7 x SS-AS) 140$\pm$45 and 200$\pm$50 [*Maillard et al.*, 1995].

1.2. VEx Era Observations

In order to understand the upper atmosphere dynamics and circulation patterns on Venus, ongoing monitoring of night airglow intensities and distributions has been conducted. New VEx observations have begun augmenting this record with measurements of key nightglow distributions (e.g. NO, O_2) and vertical structure measurements, both contributing to a growing climatology of the inferred SS-AS and RSZ wind variations [*Bougher et al.*, 2006; *Svedhem et al.*, 2009].

There are two specific instruments on VEx that focus on these measurements in this region: Spectroscopy for Investigation of Characteristics of the Atmosphere of Venus (SPICAV) and Visible and InfraRed Thermal Imaging Spectrometer (VIRTIS). SPICAV is an instrument with three different spectrometers; UV (110 - 310 nm), VIS-IR (0.7 - 1.7 μm), and Solar Occultation IR (SOIR) (2.2 - 4.3 μm). The SPICAV UV spectrometer provides night airglow (nadir and limb) observations of NO (190-270 nm) emissions, which contribute to the creation of statistical maps. Furthermore, SPICAV provides repeated measurements of vertical profiles of atmospheric density (and inferred temperatures) over $\sim$80-180 km (dayside) and $\sim$80-150 km (nightside) via stellar and solar occultations [*Bertaux et al.*, 2007]. VIRTIS is an imaging spectrometer with three channels: VIRTIS-M-VIS (imager; 0.3 - 1 μm), VIRTIS-M-IR (imager; 1 - 5 μm), and VIRTIS-H (high-resolution; 2 - 5 μm). Its observations address upper atmosphere

dynamics by: (1) measuring the 3-D temperature and derived thermal wind fields (∼60-90 km) on the nightside, and (2) mapping the O_2 IR nightglow at 1.27 μm as a tracer of the wind system over ∼90 to 130 km. Repeated measurements over several orbits provide a monitor of the IR nightglow variability at different time scales [*Drossart et al.*, 2007].

1.2.1. Temperature

An important diagnostic for upper atmosphere dynamics is the thermal structure, which is gradually being revealed by VEx. A distinctly warm layer on the nightside (∼100 km) has been discovered by stellar occultation measurements with the SPICAV instrument [*Bertaux et al.*, 2007]. The SPICAV observations suggest the temperatures between 95 and 100 km are highly variable, with an observed temperature range of ∼185 K to ∼240 K. An estimated corresponding vertical velocity was calculated to be near -0.43 m s^{-1}. These authors state that continued measurements are needed to establish a climatology of these temperatures and confirm a representative mean value in this nightside altitude region.

The Venus Express Radio Science (VeRa) observations provide temperature profiles and temperature maps of the mesosphere (below ∼90 km and above ∼50 km) [*Pätzold et al.*, 2007]. VIRTIS has measured dayside CO_2 non-local thermodynamic equilibrium (NLTE) emission at 4.3 μm up to 160 km and 2.7 μm up to 130 km. In addition, CO NLTE emission has been observed at 4.3 μm up to 120 km [*López-Valverde et al.*, 2007; *Drossart et al.*, 2007; *Gilli et al.*, 2009].

Ground-based observations have recently shown significant variations in nightside temperatures for the 95-100 km region. *Rengel et al.* [2008] published preliminary sub-millimeter measurements of CO as part of a ground-based observing campaign in support of VEx and MESSENGER. This study compared a single temperature profile from one observation (June

8, 2007) with past nightside temperature profiles and *Bertaux et al.* [2007] profiles. The *Rengel et al.* [2008] measurement of ∼185 K at 100 km is consistent with the lower range of *Bertaux et al.'s*[2007] observations. *Clancy et al.* [2008] also performed sub-millimeter line measurements of CO in support of the VEx and MESSENGER ground-based observation campaigns. Over four days (June 2, June 3, June 6, and June 11, 2007) of observations, *Clancy et al.'s*[2008] limb profiles near the equator at 8:30pm show temperatures ranging from 170 - 175 K near 100 km. These temperatures are much cooler than those of *Bertaux et al.* [2007] and *Rengel et al.* [2008]. *Clancy et al.* [2008] suggests the temperature increase is caused by a diurnal radiative balance, while *Bertaux et al.* [2007] suggests the localized warming is due to localized compressional heating from the downwelling of the day to night circulation.

Bailey et al. [2008] created nightside temperature maps from O_2 ($a^1\Delta_g$) night airglow observations with the Anglo-Australian Telescope. Their results also show night-to-night variations. For three days in July 2004, the intensity weighted mean temperature ranged from 195 to 196 K at ∼97km. During three other days in December 2005, the intensity weighted mean temperature varied from 181 to 190 K at ∼97 km. *Bailey et al.* [2008] provides a summary of available nightside temperature measurements at ∼95 km, which has been adopted in this study as Table 5. Furthermore, *Ohtsuki et al.* [2005, 2008] derived nightside temperatures from O_2 IR nightglow. They observed temperatures ranging from ∼183 to ∼193 K near 95 km. Both *Bailey et al.* [2008] and *Ohtsuki et al.* [2008] observe a correlation between the nightside warm layer and the peak O_2 IR nightglow. They made rough estimates of the vertical velocities needed to produce the warm temperature in this region; *Bailey et al.* [2008] calculated -0.2 m s^{-1} and *Ohtsuki et al.* [2008] calculated -0.05 m s^{-1}. Both estimates are consistent with *Bertaux et al.* [2007] observations leading them to the same conclusion; the nightside temperature enhancement is

due to localized compressional heating of downwelling gas from the global thermospheric circulation. With these observations, a possible range of variability of the nightside temperatures in the upper mesosphere can be assembled.

The Venus International Reference Atmosphere (VIRA), a model based on PVO Infrared Radiometer (OIR) and probe deceleration data, gives a temperature of 168 K at 95 km [*Seiff et al.*, 1985] for latitude $<30^{\circ}$. This is much cooler than what is currently being observed. However, it should be noted that VIRA is a diurnally averaged empirical model making use of only a few profiles from select probe locations. Furthermore, *Seiff et al.* [1985] states that above 95 km a diurnally-averaged model will only be accurate within 10 K.

1.2.2. Night Airglow

Nightglow distribution maps provide important constraints in modeling Venus' atmospheric dynamics. Sufficient observations from May 16, 2006 to April 7, 2007 (1225 images) were used to create an averaged statistical map (averaged spatially and temporally) of the O_2 IR night airglow [*Gérard et al.*, 2008b]. Their results show the maximum emission near $\sim$3 MR and the mean hemispheric vertical intensity at 1.3 MR. The limb observations indicate a production peak for the nightglow near 96 km but the peak can range from $\sim$90 - 110 km. Due to the trajectory of VEx, the southern hemisphere is mainly sampled for the O_2 IR night airglow. Nevertheless, previous observations discussed in section 1.1 strongly indicate the nightglow to concentrate near the equator at midnight. Recently, *Soret et al.* [2011] re-compiled the VIRTIS-M data and merged the nadir and the limb O_2 nightglow observations. Their results confirm that the bright spot is statistically centered near midnight on the equator. It has a maximum local intensity of 1.6 MR and a hemispheric average of 0.47 MR. These values are less than previously published by *Gérard et al.* [2008b], who subtracted a smaller amount of thermal background emission at

1.27 micron from the nadir observations. The mean value for the O peak density derived from the Abel inversion of the O_2 emission limb profiles is about 2 x 10^{11} cm^{-3} with a mean altitude of 103 - 104 km [*Gérard et al.*, 2009a; *Soret et al.*, 2011]. Individual limb profiles revealed the O density peak altitude to range between 95-115 km and the density peak to vary between 1 - 5 x 10^{11} cm^{-3}.

Alternatively, *Piccioni et al.* [2009] used VIRTIS limb measurements from 42 orbits to study the statistical characteristics of the 1.27 micron emission. From the analyzed retrieved profiles, the peak altitude of the volume emission rate is observed between 95 and 100 km with a mean of 97$\pm$2.5 km. This is very similar to *Gérard et al.* [2010] who analyzed 1843 limb profiles and found an average peak brightness along the line of sight of 28$\pm$23 MR at 96$\pm$2.7 km. In addition, a mean total vertical emission rate was calculated as 0.52 MR [*Piccioni et al.*, 2009]. *Piccioni et al.* [2009] constructed a distribution map from 880 orbits with observations that had emergence angles less than 80°. The localized peak vertical emission rate was 1.2 MR located at midnight and was slightly south of the equator. While the mean total vertical emission rate is very similar to the hemispheric average value from *Soret et al.* [2011], the localized peak intensity is reduced but within ranges previously observed. Finally, from visually tracking the O_2 IR nightglow brightest features, mean zonal and meridional velocities can be estimated [*Hueso et al.*, 2008].

The NO Ultraviolet (UV) night airglow has been measured by SPICAV, the UV spectrometer, thus far with rather limited spatial and temporal coverage. Statistical mean maps (composed of spatially and temporally averaged observed emissions) of the NO nightglow are presently being constructed [*Cox*, 2010]. SPICAV has made limb observations in both the δ (190-240 nm) and γ (225-270 nm) bands. For *Gérard et al.* [2008c], only 17 SPICAV orbits and 201 SPICAV

limb scans have been obtained providing acceptable NO UV night airglow limb profiles. These orbits already show large fluctuations in emission intensity and location. Early results from nadir observations with SPICAV [*Cox*, 2010] confirm the pattern previously observed at solar maximum with Pioneer Venus, (i.e. the statistically averaged NO UV nightglow emission peaks near the equator around 02:00 LT) [*Stewart et al.*, 1980].

VEx observations have begun to characterize the variability of the two (O_2 IR and NO UV) nightglow layers (i.e. both horizontal and vertical distributions) [*Hueso et al.*, 2008; *Piccioni et al.*, 2008; *Gérard et al.*, 2008b, c, 2009a, b, 2010]. The O_2 nightglow statistical bright emission has been observed from 95 - 105 km, ranging from 22:00 - 01:00 LT, at latitudes from 30°N to 20°S, with corresponding varying vertical intensities 0.5 MR to 3 MR. The NO nightglow has been observed from 95 - 132 km, ranging from 22:00 - 03:00 LT, located at 30°S to 60°N, with varying vertical intensities of 1 - 6 kR. These changes have been seen on very short timescales. See section 4.2 and 4.3 for more discussion of the observed variability.

Furthermore, *Gérard et al.* [2009b] have shown the first concurrent observations of the O_2 IR and NO UV night airglow with VIRTIS and SPICAV data. They concluded that the two nightglow emissions are not spatially correlated, giving rise to the idea that each emission is controlled by different dynamical processes [*Collet et al.*, 2010]. Recent publications [*Gérard et al.*, 2008b, c, 2009a, b, 2010; *Bertaux et al.*, 2007; *Piccioni et al.*, 2009] detailing observations made by these instruments will be discussed later in section 4.

Finally, the OH IR nightglow on Venus was first observed with VIRTIS on VEx by *Piccioni et al.* [2008]. The Meinel bands of (1-0) at 2.8 μm, (2-1) at 2.94 μm, and (2-0) at 1.43 μm were identified with evidence of additional bands in the Δv = 1 sequence. Due to the weak emission, the nightglow is only observed at the limb. The limb intensity for the (1-0) band was 0.88$\pm$0.09

MR located at 96±2 km [*Piccioni et al.*, 2008]. Additionally, *Krasnopolsky* [2010] observed the OH IR nightglow for the first time from the ground. He observed the (1-0) P1(4.5) line at 2.8 μm and (2-1) Q1(1.5) line at 2.94 μm nightglow lines. The observed slant intensities at 21:30 LT were 7.2±1.8 kR and <1.4 kR, respectively. Furthermore, at 04:00 LT the intensities were 15.5±2 kR and 4.7±1 kR, respectively. Both of these OH IR nightglow emissions peaked near 100 km.

The VEx OH IR data has been studied by *Gérard et al.* [2010] for correlations between the OH (Δv = 1) and the O_2 IR nightglow emissions and also by *Soret et al.* [2010] to determine the global distribution of OH (Δv = 1). *Gérard et al.* [2010] conducted a preliminary study and found an average brightness near 0.41±0.37 MR peaking at 95.3±3 km. A correlation with the O_2 IR nightglow was noted. More recently, *Soret et al.* [2010] has utilized 3328 limb profiles to find a mean peak of the OH (Δv = 1) emission of $0.35^{+0.53}_{-0.21}$ MR with a location near 96.4±5 km. The intensity is highly variable; i.e. it has been observed as low as <20 kR and as high as 2 MR [*Soret et al.*, 2010]. In addition, the intensity tends to be higher near the antisolar point rather than towards the poles. *Soret et al.* [2010] also noted a correlation of the OH IR and the O_2 IR nightglow emissions. This is anticipated since both nightglows production mechanisms are dependent on the same reactant, atomic O, which is created on the dayside and transported to the nightside by the global wind system.

1.2.3. Wind Observations

The cloud morphology is also being monitored by VIRTIS and the Venus Monitoring Camera (VMC) in the UV to help provide more information about the dynamics of Venus' atmosphere. Sequences of images are being used to track the motions of cloud features. Derived wind speeds near the cloud tops (50 - 70 km) can be deduced from the motion of cloud features [*Markiewicz*

et al., 2007; *Sánchez-Lavega et al.*, 2008; *Moissl et al.*, 2009]. The VIRTIS instrument made wind measurements from cloud tracking at three different altitudes layers in the Southern hemisphere. At the cloud tops ($\sim$66 km), near low latitudes, the zonal winds were measured to be westward at 105 m s^{-1} and nearly constant with respect to latitude [*Sánchez-Lavega et al.*, 2008]. The cloud base ($\sim$47 km) winds were measured to be 60 - 70 m s^{-1}. The zonal winds at higher latitudes decreased poleward and values were lower than 15 m s^{-1} [*Sánchez-Lavega et al.*, 2008]. The more recent discussion by *Moissl et al.* [2009] used observations from VMC and VIRTIS. *Moissl et al.* [2009] claimed, at latitudes poleward of 60°S, winds are difficult to track because of low contrast and scarcity of features. However, they continue to collect data and extend the latitudinal coverage [*Moissl et al.*, 2009].

Alternatively, *Sornig et al.* [2008] used the CO_2 10-μm infrared heterodyne spectroscopy technique in 2007 and made ground-based observations at the equator and at higher latitudes along the west limb (subsolar meridian). At the equator near 110 km, weak RSZ winds were measured (3 ± 7 m s^{-1}) while stronger zonal winds were obtained at higher latitudes (32 ± 4 m s^{-1}). They also retrieved a smaller SS-AS wind (52 ± 18 m s^{-1}) compared to previous measurements by *Goldstein et al.* [1991]. *Clancy et al.* [2008] used CO sub-mm measurements to derive zonal winds over an altitude range of $\sim$80 - 110 km. Due to their observing geometry, they were unable to separate the RSZ and SS-AS components, but derived total zonal winds of 195 ± 70 and 235 ± 70 m s^{-1} from two observing days in a latitude range of 30°S-30°N at the evening terminator (14:00 - 22:00 LT). Another method used to measure the winds of Venus from Earth makes use of visible Fraunhofer line scattering by Venus' cloud tops, which *Widemann et al.* [2008] used to obtain measurements at the equator and near 68 km. Their mean wind speed,

averaged over four days, of the zonal winds at the cloud tops was 104±10 m s^{-1}. This velocity is consistent with UV cloud tracking measurements.

Overall, it can be discerned from the available wind measurements the RSZ winds decrease on average from the cloud tops to ∼110 km. However there are large variations in the RSZ winds over 70 - 110 km altitude range. By examining observations near the cloud top region (60 - 70 km), an average zonal wind velocity is ∼100 m s^{-1}. Investigating the altitude range of ∼100 to 105 km, both RSZ and SS-AS winds are highly variable, ranging from ∼0 to 130 m s^{-1} and up to 300 m s^{-1}, respectively. At 110 km, the general trend shows the RSZ winds are present but are usually weak, while the SS-AS winds are ∼120 m s^{-1}. This provides strong evidence of Venus' highly varying winds and complex dynamics between ∼70 km and 110 km. It is important to obtain wind measurements at various local times in order to validate global circulation models, which help to provide a better overall understanding of Venus' upper atmosphere. More information on ground-based wind measurements can be found in *Lellouch et al.* [1997], *Bougher et al.* [2006], and *Sornig et al.* [2008].

1.2.4. Wave Observations

Perturbations in density, temperature, and cloud structures are observed by VEx and are thought to be caused by a source of variability in Venus' upper atmosphere. The actual source of these perturbations is unknown; however gravity waves are commonly implicated. Specifically, VIRTIS has detected perturbations in CO_2 NLTE 4.3 μm emissions [*Garcia et al.*, 2009]; where this emission originates in an altitude range of ∼110 km to 140 km. From these observations they are able to obtain wave structures with horizontal wavelengths ranging from 90 - 400 km. Additionally, derived horizontal phase velocities (magnitude and direction) are consistent between orbits and are on average of 70 m s^{-1} westward and 30 m s^{-1} northward [*Garcia*

et al., 2009]. *Garcia et al.* [2009] claim these observed waves are generated from the polar vortex. Moreover, VIRTIS and VMC observed visible trains of oscillating cloud brightness in the UV for an upper cloud layer ($\sim$66 km) on the dayside and from thermal radiation for the lower cloud layer on the nightside [*Peralta et al.*, 2008]. Wavelengths and phase speeds are also derived from these observations. *Peralta et al.* [2008] observed wavelengths of 60 - 150 km, which propagate westward with phase velocities similar to the zonal flow and are confined to horizontal wave packets of 400 to 1800 km. They find no correlation between the waves and surface topography, latitude, LT, or wind structure. The perturbations in these observations help provide information on potential waves mechanisms in Venus' atmosphere.

1.3. This Study

This study is focused upon general circulation model (GCM) analysis and interpretation of select recent observations from VEx. The selected nightglow emissions are O_2 IR (1.27 μm) and NO UV (190-270 nm); they serve as effective tracers of Venus' middle and upper atmosphere circulation due to their brightness. Nightside temperatures are also an important diagnostic for the circulation of the upper atmosphere. The National Center for Atmospheric Research (NCAR) Venus Thermospheric General Circulation Model (VTGCM) will be utilized, since it now spans the altitude range appropriate for these night airglow emissions, $\sim$70-200 km, on the nightside. The VTGCM has been updated and revised to produce results that are similar to upper atmosphere observations and other 1-D models.

The first objective of this study will be to define, with the available VEx data, a "mean" state for the nightside temperatures and the two nightglow emissions. The "mean" state will then be illustrated with corresponding global VTGCM simulations. Moreover, we will describe in detail how the VTGCM is used to examine the connections between the changing dynamical flows

and the averaged nightglow and thermal features. The second objective (using the VTGCM "mean" state) is to examine possible processes which may control the variability of the night airglow distributions (both horizontal and vertical) and temperatures near 100 km. The possible processes in the VTGCM are addressed using tunable parameters (the nightside eddy diffusion coefficients and the magnitude of wave drag) and two uncertain chemical reaction rates. These parameters are varied to examine how they impact the night airglow features and the global dynamics. Ultimately, these sensitivity tests will help provide a better understanding of the processes driving the variability in Venus' atmospheric dynamics.

Section 2 of this paper will discuss the VTGCM (including its recent upgrades) in detail. Section 3 will describe the results of the VTGCM simulations, which is followed by a discussion about the model results, comparison with new VEx datasets, and their implications for dynamical processes (section 4). Finally, the last section contains the main conclusions.

2. Model Description and Implementation

2.1. Model Description

The VTGCM is a 3-D, fourth-order, centered finite-difference, hydrodynamic model of the Venus upper atmosphere [e.g. *Bougher et al.*, 1988] which is based on the NCAR terrestrial Thermospheric Ionosphere General Circulation Model (TIGCM). VTGCM revisions and improvements have been documented over nearly 2-decades [see *Bougher et al.*, 1988, 1990, 1997, 1999, 2002, 2008; *Bougher and Borucki*, 1994; *Zhang et al.*, 1996]. The VTGCM code has recently been re-constructed on a new computer platform, the NCAR IBM/SP super computers [*Brecht et al.*, 2007, 2009]. This new VTGCM code makes efficient use of 4 to 32-processors in a multi-tasking environment. A parallel dynamical solver is implemented, for which assigned 2-D (latitude versus longitude) blocks spanning all altitudes are distributed

over the globe (and these processors) to reduce the overall clock time for calculations. The new VTGCM has the capability of modeling both hemispheres, instead of mirroring one to the other, enabling small Venus seasonal effects to be simulated. Subroutines from the previous VTGCM code [see *Bougher et al.*, 1988, 1990; *Bougher and Borucki*, 1994] are modified to accommodate the new array structure. The EUV-UV heating, ionization, and dissociation routines are now based on a slant column integration scheme that is optimized; this routine is called every model time-step.

The VTGCM solves the time-dependent primitive equations for the neutral atmosphere. The diagnostic equations (hydrostatic and continuity) provide geopotential and vertical motion. Additionally, the prognostic equations (thermodynamic, eastward momentum, northward momentum, and composition) are solved for steady-state solutions for the temperature, zonal (eastward) velocity, meridional (northward) velocity, and mass mixing ratio of specific species. The VTGCM composition includes major species (CO_2, CO, O, and N_2), minor species (O_2, N(^{4}S), N(^{2}D), and NO), and dayside photochemical ions (CO_2^+, O_2^+, O^+, and NO^+). These equations have been described in detail by *Bougher et al.* [1988]; primed (perturbation) values have now been replaced by total field values. The model covers a 5° by 5° latitude-longitude grid, with 69 evenly-spaced log-pressure levels in the vertical from z_p = -16 to z_p = 18 ($z_p = \ln(P_o/P)$; P_o = 5 x 10^{-3} μbar), and extending from approximately $\sim$70 to 300 km ($\sim$70 to 200 km) at local noon (midnight). The latitudinal points are placed at $\pm$2.5° - $\pm$87.5° in both directions (north and south). Currently, a 30-second time-step is utilized for all new VTGCM simulations to satisfy the Courant-Friedrichs-Lewy (CFL) stability criterion. Dayside O and CO sources arise primarily from CO_2 net dissociation and ion-neutral chemical reactions. The VTGCM ion-neutral chemistry is updated based upon the chemical reactions and rates of *Fox and Sung* [2001]. The

model can be used to examine Venus' thermospheric structure and winds from solar maximum to solar minimum EUV-UV flux conditions. In addition, the VTGCM is designed to calculate O_2 IR (1.27 microns) [*Bougher and Borucki*, 1994] and NO UV (δ band 190-290 nm and γ band 225-270 nm) [*Bougher et al.*, 1990] nightglow distributions for comparison with various Venera, PVO, VEx, and ground-based measurements (see section 2.2.3 for more details on the nightglow calculation assumptions).

2.2. Model Implementation

2.2.1. CO_2 15-micron Cooling, Wave Drag, and Eddy Diffusion

Formulations for CO_2 15-micron cooling, wave drag, and eddy diffusion are incorporated into the VTGCM [e.g. *Bougher et al.*, 1988]. CO_2 15-micron emission is known to be enhanced by collisions with O-atoms, providing increased cooling in NLTE regions of the upper atmosphere [see *Bougher et al.*, 1994; *Kasprzak et al.*, 1997]. The corresponding collisional relaxation rate adopted for typical benchmark VTGCM simulations is 3 x 10^{-12} cm^3 s^{-1} at 300 K [*Bougher et al.*, 1999]. This value provides strong CO_2 15-micron cooling that is consistent with the use of EUV-UV heating efficiencies of $\sim$20-22%, which are in agreement with detailed offline heating efficiency calculations of *Fox* [1988].

Sub-grid scale processes (i.e. eddy diffusion, viscosity, conduction, and wave drag) are not self-consistently formulated in the VTGCM, but rather parameterized using standard aeronomical formulations. For instance, Rayleigh friction is adopted to parameterize wave drag effects on the mean flow; this drag is thought to result from gravity wave momentum deposition. In particular, $F_{drag} = \lambda_{RF}$ (u - u_{SR}) where λ_{RF} is a wave drag damping rate, u is the calculated zonal wind, and u_{SR} is the specified zonal wind speed to approximate the RSZ wind [*Bougher et al.*, 1988]. The maximum u_{SR} value is set to 75 m s^{-1}. The wave drag damping rate is ex-

pressed as $\lambda_{RF} = \lambda_o \sqrt{\frac{P_{break}}{P}}$; where λ_o is the maximum λ_{RF} (λ_o = 0.5 x 10^{-4} s^{-1}) and P_{break} is the breaking level (P_{break} = 2.24 x 10^{-2} μbar). The λ_{RF} and u_{SR} terms are based upon observations with a specified exponential profile dependent on cos(latitude) which is empirically found to best match PVO and VEx observations. The realized u_{SR} profile near the equator is shown in Figure 8c. The resulting F_{drag} term is then added to the momentum equation.

Gravity wave drag formulations have been used to simulate possible activity in Venus' atmosphere [*Zhang et al.*, 1996]; new gravity wave parameters derived from VEx observations will help constrain these formulations [e.g. *Markiewicz et al.*, 2007; *Sánchez-Lavega et al.*, 2008; *Garcia et al.*, 2009]. For more detail on the Rayleigh friction and gravity wave drag formulations see *Bougher et al.* [1988].

The eddy diffusion coefficient is prescribed in the form $K = \frac{A}{\sqrt{n}}$ with units of cm^2s^{-1} where *n* is the total number density and *A* is a constant estimated to be 5.5 x 10^{12} for the nightside [*von Zahn et al.*, 1979]. The nightside eddy diffusion has a maximum of 1 x 10^7 cm^2s^{-1} and the dayside has a constant value for the entire upper atmosphere of 1 x 10^6 cm^2s^{-1}. The nightside eddy diffusion profile is represented as the "best case" profile in Figure 15. The eddy diffusion coefficient utilized is smaller than used previously in 1-D models due to the expanded role of mixing by the VTGCM global wind system [e.g. *von Zahn et al.*, 1979; *Stewart et al.*, 1980; *Gérard et al.*, 1981; *Massie et al.*, 1983; *Drossart et al.*, 2007; *Gérard et al.*, 2008b]. The incorporation of different dayside and nightside eddy diffusion profiles is based upon PVO density observations; i.e. the nightside densities are observed to vary $\pm 50\%$ which was found to be approximately three times more than on the dayside [*Keating et al.*, 1980, 1985; *Kasprzak et al.*, 1988, 1993]. Currently in the VTGCM, the dayside eddy diffusion profile is used from SZA = 0° - 105° and the nightside eddy diffusion profile is used from SZA = 106° - 180°.

The associated boundary conditions are as follows. The top boundary assumes $\frac{dT}{dz}$ = 0, $\frac{du}{dz}$ = $\frac{dv}{dz}$ =$\frac{dw}{dz}$ = 0 and the composition is in diffusive equilibrium, thus LΨ = 0. The bottom boundary presently assumes all winds are zero and a temperature value of 230 K is prescribed. A return flow (night to day) is neglected, thus Ψ_O = 1.2 x 10^{-10} [*Yung and Demore*, 1982] and Ψ_{CO} = 5.8 x 10^{-5} (where Ψ is mass mixing ratio) and N_2 is calculated as a simple diffusive equilibrium constituent above z_p=0 (the homopause). The O boundary condition does not allow O escape due to the presence of the low altitude trace species, which shorten the O lifetime dramatically when compared to the eddy diffusion time scale near 80 km. The mass mixing ratio for CO_2 is derived by Ψ_{CO_2} = 1.0 - Ψ_{CO} - Ψ_O - Ψ_{N_2}. The minor species lower boundary values are set according to global averaged values given by *Yung and Demore* [1982] and the ions are in photochemical equilibrium. The leap-frog scheme is chosen for the temporal discretization.

The most recent VTGCM model changes are crucial to properly reproduce VEx observations. The VTGCM lower boundary is now extended downward and the upper boundary is extended upward. The altitude range at local noon currently spans ∼70 km to 300 km. This insures that all the dynamical influences contributing to the NO UV and O_2 IR nightglow layers can be captured. "Exact" (line-by-line radiative transfer model) CO_2 15-micron cooling rates for a given temperature and composition profile are taken from *Roldán et al.* [2000]; cooling rates for the simulated VTGCM temperatures and species abundances are calculated (from these "exact" rates) based upon a slight modification of the parameterization scheme described previously [e.g. *Bougher et al.*, 1986]. The near-IR heating term is incorporated using offline simulated look-up tables, updated recently using *Roldán et al.* [2000] rates. *Roldán et al.* [2000] discusses the detailed NLTE radiative transfer model, which "computes the populations of more than 60 vibrational levels of the four major isotopes of CO_2, and the cooling and heating rates by more

than 90 radiative transitions". Further discussion within *Roldán et al.* [2000] compares their results with previous calculations [e.g. *Dickinson*, 1972; *Deming and Mumma*, 1983; *Gordiets and Panchenko*, 1983; *Stepanova and Shved*, 1985; *Dickinson and Bougher*, 1986] and explains the improvements in the heating and cooling rates. The most noticeable improvement from adding the new IR heating rates into the VTGCM is found in the doubling of the 4.3 micron heating around 120 km on the dayside.

2.2.2. NO UV Nightglow and N-production

The NO UV nightglow emission and N-atom production have been updated with the application of solar photodissociation and photoelectron dissociation rates of N_2 for solar minimum or maximum conditions, based upon detailed 1-D model simulations by J. -C. Gérard [e.g. *Gérard et al.*, 2008a]. In these calculations, the cross sections for the N_2 dissociation by solar UV photons are obtained as the difference between the total absorption and the ionization cross sections. High resolution cross sections and predissociation probabilities are needed to quantitatively model the production of atomic nitrogen. *Fox et al.* [2008] have stated this to be important for the highly structured regions of the N_2 photoabsorption spectrum shortward of the ionization threshold at 79.6 nm where predissociation and autoionization compete. Currently high resolution cross sections are being measured and predissociation lifetimes are being calculated. Even with this progress there is still insufficient information (e. g. branching ratios) to compute the production rates of atomic nitrogen or the total photodissociation rate of N_2 [*Fox et al.*, 2008]. Instead, the use of lower resolution solar fluxes and cross sections can provide accuracy to a "factor of only a few" [*Fox et al.*, 2008]. More accurate rates are presently approximated within the VTGCM by tripling the rates calculated for large wavelength bins (low

resolution). These new N-production rates provide proper chemical sources of atomic nitrogen on the dayside coupled with transport to the nightside to produce the NO UV night airglow.

2.2.3. Updated Airglow Chemistry

Another VTGCM modification involves updates of the night airglow chemistry with recent reaction rates and yields. Illustrated in Figure 2 are sources and sinks for atomic oxygen on the dayside. The selected reactions are listed in order of decreasing importance for atomic oxygen production:

$$CO_2 + h\nu \rightarrow CO + O \quad \text{(RK1)}$$

$$O_2^+ + e \rightarrow O + O \quad \text{(R7)}$$

$$CO_2^+ + e \rightarrow CO + O \quad \text{(R8)}$$

$$O_2 + h\nu \rightarrow O + O \quad \text{(RK2)}$$

There are two altitude regions where O is produced. The production peaks for reactions RK1 and RK2 are near 110 km, while reactions R7 and R8 peak near 140 km. The two different altitude source regions are important for the production of the O_2 IR night airglow and the NO UV nightglow, respectively.

Figure 3 illustrates the chemical processes, sources and sinks, controlling the dayside atomic nitrogen abundance [*Bougher et al.*, 1990]. The main sources of atomic nitrogen come from photodissociation and photoelectron impact of molecular nitrogen (see section 2.2.2). These reactions can supply both ground state and excited atomic nitrogen, N(^{4}S) and N(^{2}D), respectively. The branching ratio used for N(^{2}D) is f=0.5 [*Bougher et al.*, 1990]. There are four selected reactions that regulate dayside atomic nitrogen, plus N(^{2}D) quenching by atomic oxygen and carbon monoxide:

$$N(^2D) + CO_2 \rightarrow NO + CO \quad \text{(R10)}$$

$$N(^4S) + O_2^+ \rightarrow NO^+ + O \quad \text{(R14)}$$

$$NO + N(^4S) \rightarrow N_2 + O \quad \text{(R15)}$$

$$NO^+ + e \rightarrow gN(^2D) + (1-g)N(^4S) \quad \text{(R20)}$$

The dissociative recombination of NO^+ also supplies ground state and excited atomic nitrogen species; thus a branching ratio of g=0.75 is used for N(^{2}D) [*Bougher et al.*, 1990]. The dayside atomic nitrogen production peak is located near the ionospheric peak at 140 km.

The two dayside produced atomic species, nitrogen and oxygen, are subject to transport by the global thermospheric circulation. Upwelling occurs on the dayside with strong cross terminator horizontal flow and downwelling on the nightside. These species follow the global circulation streamlines to the nightside at different altitudes. The stream lines closely follow constant pressure surfaces. Therefore, the streamlines decrease in altitude from day to night due to the colder nightside temperatures and downwelling of the converging global circulation. The main chemical reaction for O_2 IR night airglow production and the main chemical loss of atomic oxygen on the nightside (above $\sim$90 km) is:

$$O + O + CO_2 \rightarrow O_2^* + M \quad \text{(R1)}$$

The O_2 IR emission is assumed to be optically thin and uses a typical yield of 75$\%$ [e.g. *Gérard et al.*, 2008b] for the O_2 IR production. There are other estimated yields, such as *Crisp et al.* [1996], which are based on laboratory studies. They found yields of 0.63$\pm$0.19 for M = N_2 and $\sim$0.6-0.75 for M = CO_2. Another estimated yield was presented by *Huestis* [2002]; values of 0.94 - 0.99 were generated for M = N_2 and M = CO_2 by combining laboratory studies and atmospheric studies. The formulation for the O_2 ($^1\Delta$) 1.27 μm emission is retained from *Bougher and Borucki* [1994]. The main chemical loss on the nightside for N(^{4}S) and the main chemical

reaction for production of the NO UV night airglow is:

$$N(^4S) + O \rightarrow NO^* \quad \text{(R16)}$$

Reaction R16 provides emissions for both delta and gamma bands. For the NO UV emission it is assumed to be optically thin and utilizes a yield of 100%. See *Bougher et al.* [1990] for more details. This reaction competes strongly with reaction R15.

$$N(^4S) + NO \rightarrow N_2 + O \quad \text{(R15)}$$

For a summary of all the reactions, reaction rates, and yields used within the VTGCM for atomic oxygen and atomic nitrogen see Table 1.

2.3. Re-evaluated Chemical Rate Coefficients

In this section two reaction rates will be discussed, R1 (O + O + M) and R17 (N + O + M). Preliminary laboratory measurements and evaluations of these rates are currently available, resulting in updated rates for use in the new VTGCM simulations (see Table 2).

Research previously published in the literature uses the rate constant of R1 = 2.75 x 10^{-32} cm^6 s^{-1} [*Gérard et al.*, 2008c; *Nair et al.*, 1994; *Campbell and Gray*, 1973] for Venus and Mars where CO_2 is the background atmosphere. However, this rate constant has only been properly evaluated for the case of the Earth, which has a background atmosphere of N_2, based on *Campbell and Gray* [1973]. This rate for M = N_2 is then multiplied by a factor of 2.5 [*Nair et al.*, 1994] for an estimation of the relative efficiency of CO_2 (versus N_2) as the third body. The 2.5 factor is very weakly supported and documented. *Nair et al.* [1994] provide no numerical details about how they derived their factor of 2.5 (*Huestis*, private communication, 2010). Recently, a preliminary rate coefficient has been measured and suggested for a predominantly CO_2 background atmosphere [*Huestis*, private communication, 2010; *Jamieson et al.*, 2009a, b].

This preliminary rate, R1 = 1.8 x 10^{-32} cm^3 s^{-1} at 200 K, is slower than what has been used in the past. This implies that 3-body recombination should occur at a lower altitude (higher CO_2 density) in the Venus atmosphere, with a corresponding lowered O_2 nightglow layer as well. A sensitivity test has been completed using the preliminary (test) rate in the VTGCM and the model results are discussed in section 3.3.3.

The other rate recently revisited is R17 (see Table 2). In previous VTGCM simulations [*Bougher et al.*, 1990] a rate of 1.1 x 10^{-32} $(300/T_n)^{0.5}$ cm^6 s^{-1} was used from *Stewart and Barth* [1979]. Upon closer inspection, the *Stewart and Barth* [1979] rate is based upon measurements conducted by *Baulch et al.* [1973], where M = N_2. As stated above, CO_2 is a more efficient third body than N_2. Previous measurements were also conducted with a CO_2 background for two different temperatures [*Campbell and Thrush*, 1966]. One measurement for 196 K gave a rate of 2.26 x 10^{-32} cm^6 s^{-1} and the other for 298 K gave a rate of 1.83 x 10^{-32} cm^6 s^{-1}. For our new VTGCM, a temperature dependent rate was derived using these two measurements, giving a rate of 1.83 x 10^{-32} $(298/T_n)^{0.5}$ cm^6 s^{-1}, where T_n is the neutral temperature. The change in this rate does not impact the O_2 IR nightglow but slightly changes the NO UV nightglow. See section 3.3.3 for the VTGCM model results and section 4.2 for comparisons to available observations.

2.4. Chemical Trace Species at lower altitudes

A final chemical update to the VTGCM is implemented by adding nightside profiles of specific chemical trace species. *Krasnopolsky's* [2010] calculations suggest that other odd-O loss processes may be important on the nightside involving trace species that impact nightglow emissions [*Krasnopolsky*, 2010]. Trace species have been added to the VTGCM before, but the profiles used were diurnally averaged [*Bougher and Borucki*, 1994; *Yung and Demore*, 1982]. At

that time, trace species did make a noteable difference in the O density profiles at low thermospheric altitudes [see figure 8 in *Bougher and Borucki*, 1994].

Currently, single density profiles of trace species (Cl, Cl_2, ClCO, ClO, H_2, HCl, HO_2, O_3, OH) from an altitude of $\sim$70 km to 130 km for the nightside have been extracted from *Krasnopolsky* [2010] figure 8 and incorporated into the nightside of the VTGCM. *Krasnopolsky* [2010] employs a 1-D photochemical model that is tuned for nightside conditions (photolysis is not involved) which includes 61 reactions and 24 species. As stated in *Krasnopolsky* [2010], the model results are within observational ranges for the O_2 IR, NO UV, and OH IR nightglow emissions and peak altitudes. Therefore, VTGCM reaction rates involving these trace species are taken from table 4 in *Krasnopolsky* [2010] with additional reaction rates from *Yung and Demore* [1982].

It is appropriate not to carry these trace species dynamically in the VTGCM. This is justified because in the region where the trace species greatly impact the atmospheric chemistry, they have very short chemical lifetimes with respect to the dynamics. When these trace species were added to the VTGCM, they made a noticeable difference in the nightglow layers (see section 3.3.4). They provide additional loss terms for the O chemistry at the lower altitudes (below 90 km) and help define a narrower O density layer. This directly impacts the O_2 IR nightglow and indirectly impacts the NO UV nightglow. Without these trace species, the chemistry is incomplete in the VTGCM and the varying nightglow emission layers cannot be properly simulated for comparison to available datasets.

3. VTGCM Simulation Results

This section outlines the inputs specified for a VTGCM best case (also referred to as a "mean" simulation) and illustrates specific results for the Venus upper atmosphere structure and dynam-

ics (e.g. temperatures, winds, O and N(^{4}S) densities, O_2 IR and NO UV nightglow emissions). A "mean" simulation is computed using static input parameters (section 3.1) and boundary conditions (section 2.2), and the model is run to a steady-state solution. Steady-state is determined by the difference between the last simulated model day and the previous simulated model day having a percent difference of less than 2% for all prognostic fields. For the VTGCM, a typical simulation takes about 9 simulated Earth days to reach such a steady-state condition starting from a symmetric wind condition. Once a realistic "mean" simulation is completed, sensitivity tests are performed with two adjustable parameters (maximum nightside eddy diffusion and wave drag impacting the global wind system). In addition, an evaluation is made of the chemical impacts by varying key reaction rates and adding chemical trace species. The purpose of this section is to examine the VTGCM "mean" simulation results using VEx parameters and to demonstrate the VTGCM sensitivity to specific input parameters. Data-model comparison will be conducted in section 4, specifically focused on VEx measurements.

3.1. "Mean" Simulation - Parameters for VEx conditions

In order to simulate mean conditions for the Venus' middle and upper atmospheres during VEx sampling periods, the VTGCM is run with solar minimum fluxes (F10.7 = 70 at 1 AU), a nightside maximum eddy diffusion of 1.0 x 10^7 cm^2 s^{-1} and a wave drag parameter (λ_{RF}) of 0.5 x 10^{-4} s^{-1}. Mean VEx conditions are best captured by VEx statistically averaged mean nightglow emission maps. Presently, the O_2 IR statistical map (observed emissions averaged spatially and temporally) exists and is used for data-model comparisons for mean conditions [*Gérard et al.*, 2008b; *Piccioni et al.*, 2009; *Soret et al.*, 2011]. Other maps have been created for single orbits and are being used to observe the nightglow morphology [*Hueso et al.*, 2008].

The NO UV statistical map is being developed and has provided initial information on the averaged nightglow morphology [*Cox*, 2010].

3.2. "Mean" Simulation - Results

The measured thermal structure of Venus' upper atmosphere has several interesting characteristics that the VTGCM reproduces in its "mean" simulation. Figure 4 represents the simulated thermal structure near the equator at 2.5°N. At the exobase ($\sim$190 km), temperatures range from 238 K on the dayside to 114 K on the nightside. At 12:00 LT near 112 km is a warm region, about 207 K, created by near IR (i.e. mostly 4.3 μm) heating. Near 00:00 LT, a warm region is produced at 103 km with a simulated temperature around 188 K. Figure 5 illustrates the heating and cooling rates at 12:00 LT and 00:00 LT. On the dayside, there is mostly a radiative balance with small influences from dynamics. However, on the nightside the temperatures are regulated by the magnitude of dynamical terms.

Figure 6a shows a 1D representation of the nightside temperature profile. The nightside warm region is associated with the dayside warm region (in the lower thermosphere) and the resulting day-to-night global circulation, which produces dynamical heating near midnight. The total dynamical heating rate (adiabatic + total (horizontal + vertical) advection) at 103 km near the anti-solar point is 64 K/day (see Figure 6b). This heating rate is dominated by adiabatic heating at 103 km near midnight. Above 130 km on the nightside, temperatures remain cold at 114 K. Thus the new VTGCM simultaneously reproduces the nightside cryosphere ($>$130 km) characterized by PVO observations and reproduced by previous modeling efforts [*Keating et al.*, 1979; *Bougher et al.*, 1997], and the observed warm nightside temperature near 100 km at midnight (see section 4.1).

The neutral zonal winds near the equator are illustrated in Figure 7. The evening terminator (ET) winds are 143 m s^{-1} at ∼110 km, 202 m s^{-1} at ∼120 km, and reach a maximum at 314 m s^{-1} near 180 km. The morning terminator (MT) winds are -135 m s^{-1} near 110 km, -130 m s^{-1} near 120 km, and are maximum at -191 m s^{-1} near 172 km. The ET winds are faster than the MT winds since the drag term is prescribed asymmetrically in local time in order to mimic the observed upper atmosphere RSZ winds (see Figure 8c). It is noteworthy that the VTGCM captures the shift in the convergence of the flow away from midnight and toward the morning terminator above 110 km. The simulated wind magnitudes are within observed ranges, see the discussion in sections 1.1 and 1.2.3. At this time, it is difficult to make detailed, direct comparisons with wind observations due to the high variability of the wind magnitudes and the geometry used to make these measurements. This VTGCM wind system provides a downward vertical velocity at midnight of ∼0.1 m s^{-1} at 105 km, which is consistent with other estimates in the literature [*Bailey et al.*, 2008; *Ohtsuki et al.*, 2008] but lower than the *Bertaux et al.* [2007] value of 0.43 m s^{-1}.

Figure 8 shows the ET and MT total zonal wind profiles and the prescribed RSZ wind profile near the equator (prescribed using the u_{SR} term in the wave drag equation). The difference between the terminator symmetric and asymmetric total zonal wind profiles reflects the impact of the prescribed RSZ wind profile (see Figure 8c). The RSZ profile is applied globally with respect to height and cos(latitude), and plays a crucial part in producing the nightglow distributions (i.e. the local time location of the peak emission). In order for the O_2 IR nightglow peak intensity to be produced at midnight, the RSZ needs to be very weak (as shown in Figure 8c), up to ∼110 km. By contrast, for the NO UV nightglow peak intensity to be positioned near 02:00 LT, the RSZ wind has to be 30 - 60 m s^{-1}, above ∼110 km. On the dayside, N(^{4}S)

atoms are produced near ∼140 km, and subsequently are transported nightward as they follow descending pressure levels to the colder nightside. The dayside pressure at 140 km is equivalent to the pressure at ∼130 km on the nightside. For this altitude region, the RSZ wind is 60 m s^{-1} which is comparable to estimates from previous measurements [see Table 1 in *Bougher et al.*, 2006]. Conversely, O is produced near 110 km on the dayside and descends more gradually to the nightside along constant pressure surfaces owing to a weaker diurnal variation in temperatures in this region. For more details about the impacts RSZ winds have on the nightglow, see sections 4.2 and 4.3.

Another result that contributes to the validation of the chosen eddy diffusion coefficient profiles (day versus night) is shown in Figure 9. Mixing ratios from the VTGCM "mean" case (shown in black) are compared to the VTS3 empirical model values (in red) [*Hedin et al.*, 1983]. The VTS3 model is based upon PVO neutral mass spectrometer in situ measurements (mainly solar maximum conditions) obtained at low latitudes above ∼140 km and uses the hydrostatic equilibrium assumption to extrapolate mixing ratios below ∼140 km. The top panel of Figure 9 illustrates mixing ratios for O, CO, and CO_2 at LT = 12:00. Near the top of the dayside panel, the mixing ratios deviate since the VTGCM currently does not include He, which becomes dominant above ∼195 km in the VTS3. Otherwise the two models are in favorable agreement. The bottom panel of Figure 9 expresses mixing ratios for O, CO, CO_2 at LT = 00:00. The calculated mixing ratio peak altitudes and magnitudes match VTS3 values reasonably well. However, there are discrepancies near the bottom of the nightside panel. The VTS3 does not incorporate day to night transport of atomic O and trace species. In this region the VTS3 is strictly an extrapolation from higher altitudes and is used as a first order representation of the thermosphere.

Figure 10 illustrates the atomic oxygen density profiles for noon and midnight near the equator with respect to (a) log pressures and (b) altitude. Profiles in Figure 10b are provided from 80 km - 190 km to focus on the density structure near the peak. The atomic oxygen density at noon peaks at 94 km with a value of 5.5 x 10^{10} cm^{-3}, while the midnight value is 3.4 x 10^{11} cm^{-3} at 104 km. This $\sim$6 fold enhancement from day to nightside is the result of efficient transport of atomic oxygen atoms from their day side source to their nightside chemical loss at and below 104 km. The VTGCM also produces a noon time O/CO_2 mixing ratio for the dayside at 140 km of 5%. The corresponding net dayside column integrated production (at 60° SZA) for O atoms is calculated to be 2.34 x 10^{12} cm^{-2} s^{-1}.

The N(^{4}S) density profile for noon and midnight near the equator is shown with respect to log pressure in Figure 11a and with respect to altitude in Figure 11b. The altitude plot ranges from 80 km to 190 km to focus on the structure near the density peak. At noon, the peak value near the equator is 1.0 x 10^8 cm^{-3} at 136 km. The nightside density profile peaks at 1.4 x 10^8 cm^{-3} at 115 km near the equator. This 40% fold enhancement, although less pronounced than atomic oxygen, still reflects the combined effects of transport and nightside chemical destruction of atomic nitrogen at and below $\sim$110 km. This is complemented with a net dayside column integrated production at 60° SZA for N(^{4}S) of 1.58 x 10^{10} cm^{-2} s^{-1}.

The results presented in Figure 12 illustrate the maximum volume emission rate for the O_2 IR nightglow near the equator at $\sim$100 km to be 1.7 x 10^6 (photon cm^{-3} s^{-1}) with a corresponding peak vertical intensity of 1.76 MR. This peak value is near midnight in concert with the simulated global wind structure. The nightside hemispheric average (defined by a box of 60°S to 60°N and 60°E to 60°W) is $\sim$0.51 MR requiring $\sim$0.22 photons per O atom produced on the dayside and made available to the nightside for destruction. A 100% yield of the three

body reaction (O + O + CO_2) for production of O_2 IR nightglow would provide a peak vertical intensity closer to 2.37 MR and a hemispheric average of 0.63 MR.

Figure 13 illustrates the volume emission rate of the NO UV nightglow for the δ and γ bands near the equator. The maximum value is 1.2 x 10^3 (photon cm^{-3} s^{-1}) near 106 km and has a corresponding peak vertical intensity of 1.83 kR. The peak value is shifted towards the morning terminator and is located at ~01:00 LT due to the asymmetrical global winds at 106 km (see Figure 8). The nightside hemispheric intensity average is 0.68 kR. This emission requires 0.04 photons per N atom produced on the dayside and made available to the nightside for destruction. For this "mean" simulation (and incorporating a suite of standard chemical reactions and upgraded rates) the O_2 IR and NO UV night airglow layers are very close in altitude and therefore exist in a relatively similar dynamical region of the upper mesosphere and lower thermosphere.

Time scale plots provide a good measure of the processes which dominate in any given region at a given time. Figure 14 shows vertical profiles of the atomic oxygen and N(^{4}S) chemical lifetimes, eddy and molecular diffusion lifetimes, and dynamical (horizontal and vertical winds) lifetimes at 00:00 LT in units of days. The chemical lifetime is calculated as the inverse of loss frequency with atomic oxygen (or N(^{4}S)) being the chemical species of concern, since it is the major contributor for the reaction of the O_2 IR (or NO UV) night airglow. Eddy diffusion lifetime is estimated by $\tau_{eddy} = \frac{H^2}{K_{eddy}}$, where H is the mean scale height (H = $\frac{RT}{mg}$ where R = universal gas constant, T = neutral temperature, m = mean molecular weight, g = gravity), and K_{eddy} is the eddy diffusion coefficient. Above ~130 km τ_{eddy} decreases due to H increasing; this results from the increasing importance of atomic oxygen above ~130 km despite nearly constant temperatures. The molecular diffusion lifetime is calculated as $\tau_D = \frac{H^2}{D}$, where D is the molecular diffusion coefficient for O in a CO_2 atmosphere. For more details on the formulation

of *D* see *Dickinson and Ridley* [1972]. The lifetimes of eddy diffusion and molecular diffusion are equal near 127 km, resulting in a homopause at 127 km on the nightside. This homopause location (neglecting the mixing influence of the VTGCM global winds) is ∼4 km lower than 1-D model predictions of *Massie et al.* [1983], which uses a maximum eddy diffusion of 5 x 10^7 cm^2 s^{-1}. The lifetime corresponding to the horizontal wind (motion of a parcel) utilizes the wind velocity on the evening terminator; i.e. it is the location of the fastest horizontal winds and therefore a dominant contributor to the distribution of chemical species. The vertical wind lifetime is $\tau_{vertical} = \frac{H}{w}$, where $\tau_{vertical}$ is the vertical velocity lifetime and *w* is vertical velocity. Both nightglow emissions are controlled mainly by the strength of the global circulation which transports O and N(^{4}S) atoms from the dayside. In the case of the O_2 IR night airglow, the time scale plot reveals the eddy diffusion lifetime matches the O chemical lifetime at 100 km, while dynamics plays a role at higher altitudes. Therefore eddy diffusion is the dominating process in the region where the volume emission rate of the O_2 IR night airglow peaks. For N(^{4}S), the altitude of the nightglow is different from O_2 IR night airglow and it is controlled by the vertical winds. The vertical wind lifetime and the N(^{4}S) lifetime match at 105 km. Therefore the time scale plot shows the vertical velocity dominating the region where the NO UV nightglow peaks, while the eddy diffusion time scale is not competitive enough to make a significant impact on the nightglow altitude peak. If the winds are slowed down sufficiently to let eddy diffusion dominate, day to night transport of O and N atoms is inadequate to provide the source for the intense emissions of O_2 IR or NO UV nightglow observed.

3.3. Sensitivity Tests upon the "Mean" Simulation

As mentioned in the introduction (section 1), our purpose for VTGCM analysis of VEx datasets is to understand the processes controlling the variable night airglow layers. The O_2

IR and NO UV night airglow layers were subsequently examined for their sensitivity to two adjustable parameters in the VTGCM model (i.e. the maximum nightside eddy diffusion and the strength of the Rayleigh friction (impacting the global wind system)). A discussion follows about the chemical impacts on the nightglow emissions and their distributions.

3.3.1. Sensitivity Tests - Eddy Diffusion

For the eddy diffusion test, the maximum eddy diffusion coefficient is varied, consistent with the observed variation of nightside densities [e.g. *Keating et al.*, 1980; *Kasprzak et al.*, 1993]. The eddy diffusion coefficient is prescribed in the form $K = \frac{A}{\sqrt{n}}$ with units of cm^2 s^{-1} where *n* is the total number density, *A* is a constant, and *K* is the eddy diffusion coefficient (which is capped at a maximum value, *Kmax*) [*von Zahn et al.*, 1979]. Three *Kmax* values are used for the test; (a) the maximum case is 8.0 x 10^7 cm^2 s^{-1}, (b) the minimum case is 1.0 x 10^6 cm^2 s^{-1}, and (c) the best case (which corresponds to the results previously discussed in section 3.2) is 1.0 x 10^7 cm^2 s^{-1}. The eddy diffusion profiles for this study are represented in Figure 15a and the results of the sensitivity test can be seen in Table 3. Eddy diffusion proves to be a major factor in controlling the altitude of the nightglow peaks [*Bougher et al.*, 1997; *Bougher and Borucki*, 1994]. For the new VTGCM, the O_2 IR nightglow intensity is more sensitive than the NO UV nightglow to the changing eddy diffusion coefficient. The nightglow intensities also vary with respect to the location of the sources and sinks of the nightglow layer. Lower in the atmosphere, CO_2 concentrations are greater, which reduces the O_2 IR night airglow chemical sources by increasing the deactivation of the O_2 ($a^1\Delta$) state by CO_2 quenching. The NO UV nightglow intensity varies as the nightglow layer moves vertically for a similar reason, with an additional N(^{4}S) sink being:

$$N(^4S) + O + CO_2 \rightarrow NO + CO_2 \qquad \text{(R17)}$$

A larger eddy coefficient leads to reaction (R17) competing more effectively with reaction (R16) for N(^{4}S) atoms, thereby reducing the NO* source. The opposite happens when the eddy coefficient is minimized.

3.3.2. Sensitivity Tests - Wind

The wind sensitivity is related to the tunable wave drag parameter which is part of the Rayleigh friction scheme. The Rayleigh friction term is implemented to approximate gravity wave momentum drag effects. This rudimentary formulation is linearly proportional to the horizontal (2D) wind, and is added to the momentum equation thereby controlling the magnitude of the zonal and meridional winds and ultimately the magnitude of the subsiding winds near midnight. The procedure of the wind sensitivity test is similar to the eddy diffusion sensitivity test. The wave drag time scale maximum values (λ_o parameter in the wave drag equation) used are as follows; (a) the maximum case is 2 x 10^{-4} s^{-1} (providing slower winds), (b) the minimum case is 1.25 x 10^{-5} s^{-1} (providing faster winds), and (c) the best case is 0.5 x 10^{-4} s^{-1} (providing optimal winds and is used for all results previously discussed in section 3.2). The resulting evening terminator (LT = 18:00) zonal wind profile for each case is represented in Figure 15b.

Table 4 summarizes the results of the wind sensitivity study. These cases demonstrate that the intensities of the nightglow emissions are impacted more strongly than the altitude of the nightglow peaks. The stronger impact on the intensities is due to the SS-AS wind system that supplies the nightside with O and N(^{4}S) atoms transported from the dayside. The nightglow intensities respond accordingly to the strength of the winds, while the nightside N(^{4}S) peak density does not. In fact, the nightside O density and the nightside N(^{4}S) density have opposite responses to the strength of the wind. The closer the density peaks are in altitude, the greater

the loss of N(^{4}S) through reactions R15 and R16. As seen in Table 4, the weaker winds provide more N(^{4}S) (less O) on the nightside and the stronger winds yield more N(^{4}S) and O when compared to the "best case". This implies the drag term is most influential between 100 km and 110 km, where O density peaks. For the morphology of the nightglow emissions, the local time distribution is shifted toward the MT (ET) when there are stronger (weaker) winds. Therefore, the source of these atoms, and thus the nightglow peak brightness and location, directly depends on the strength of these winds.

Furthermore, it is suggested the nightside warm region is created by dynamical heating and the bottom of Table 4 illustrates the nightside warm region's sensitivity to the wind changes. The decrease in wind results in a cooler "warm" region and it peaks 9 km lower than the "best case", while a increase in the global wind system results in the opposite response.

3.3.3. Sensitivity Tests - Key Chemical Reaction Rates

For the 3-body reaction rate R1, modelers have been using a standard Earth value and multiplying it by a constant factor to enable the reaction rate to correspond to a CO_2 dominated atmosphere. Recently, this reaction has been measured in the laboratory in a CO_2 background atmosphere by *Jamieson et al.* [2009b]. In Table 2 the different reaction rates used in this sensitivity test are clearly stated. When the preliminary (test) R1 rate is used a slight impact on the O density profiles is identified ($\sim$13% increase for the peak dayside density and $\sim$12.6% increase for the peak nightside density) within the VTGCM simulations. The change from the standard R1 to the preliminary (test) R1 leaves more O available on the nightside and decreases the peak O_2 nightglow intensity to 1.68 MR. However, the peak altitude remained at 100 km. The NO UV nightglow layer remains at 106 km, but has a slight increase in intensity to 1.9 kR.

In the past, the VTGCM used an Earth based value for the 3-body reaction rate R17. This sensitivity study compares the atmospheric impacts when using this previous reaction rate (test) and a standard one based upon measurements using a CO_2 background atmosphere (see Table 2 and see section 2.3 for more details about the rates). By using the standard reaction rate (1.83 x 10^{-32} (298/T_n)$^{0.5}$ cm^6 s^{-1}), which is faster, this requires fewer N and O atoms for reaction R16 to occur at higher altitudes, thus resulting in the NO UV nightglow layer occurring higher in the atmosphere and further separated from the O_2 IR nightglow layer. When using the test reaction rate (1.1 x 10^{-32} (300/T_n)$^{0.5}$ cm^6 s^{-1}), which is slower, this leads to N and O atoms recombining lower in the atmosphere. However, application of the standard rate does not impact the NO UV nightglow layer height and the intensity increases from 1.83 kR to 1.92 kR. Reaction rate R17 is the least important loss of N(^{4}S) compared to reactions R16 and R15. Nevertheless, since R17 does impact the NO UV nightglow, this chemical reaction rate is in need of a new laboratory measurement for application to Venus.

In the literature, error bars are typically stated for measurements of chemical reaction rates. Thus, a careful examination of a range of reaction rates for odd-N chemistry was tested using the VTGCM. Little impact was observed on the altitude of the NO UV nightglow peak [*Bougher et al.*, 1990; *Fox*, 1994; *Fox and Sung*, 2001; *Krasnopolsky*, 2010]. In short, the combination of the chemical reaction rates listed in Table 1 are used to create the VTGCM "mean" case.

3.3.4. Sensitivity Tests - Chemical Trace Species

By implementing the *Krasnopolsky* [2010] night profiles of chemical trace species into the VTGCM, the density profiles and night airglow distributions were impacted. The trace species provide additional loss terms for the O chemistry below 95 km, which creates a narrower O density layer (see Figure 10). The more defined O density layer becomes more sensitive to the

dominating reactions (e.g. R1), as previously discussed, resulting in a more sensitive nightglow emission layer with respect to the eddy diffusion coefficient. The O_2 IR nightglow layer is raised a kilometer with the trace species, and the peak intensity is decreased (by 0.2 MR). The N(^{4}S) density plot changes slightly as well (see Figure 11). The NO UV nightglow is created in the region where the N(^{4}S) density layer overlaps the O density layer. Since the O density layer is more sensitive to the eddy diffusion coefficient, this also creates a more variable NO UV nightglow layer. However, the NO UV nightglow layer altitude and intensity did not change with the addition of trace species.

3.3.5. Sensitivity Tests - Conclusions

These sensitivity tests show that the wave drag parameter (impacting wind magnitudes) controls the intensity of the nightglow emissions, while eddy diffusion controls the altitude of the nightglow layers. The O_2 IR nightglow is more sensitive to eddy diffusion and the NO UV nightglow is more sensitive to the wave drag parameter (the strength of the global wind system). The key reaction rate tests revealed little impact on the nightglow layers location, but slightly impacted the intensity. The addition of chemical trace species is crucial for completeness and determining the shape of the O_2 IR nightglow emission layer. Overall, these different responses may explain (in part) the observed variability in location and intensity of the O_2 IR and NO UV nightglow emissions. Moreover, the implications of the time scale plot (see Figure 14), plus the eddy diffusion and the wind sensitivity tests, point to a dynamical explanation for the lack of correlation between these concurrently observed nightglow emissions (see section 4.3)[*Gérard et al.*, 2009b].

4. Implications and Data Model Comparisons

The latest VTGCM modeling efforts have been focused on three key VEx observations; (a) the nightside warm layer near 100 km, (b) the O_2 IR nightglow, and (c) the NO UV nightglow. Currently, the modeling of these key observations is unique because the VTGCM alone provides a self-consistent set of structural and dynamical fields (i.e. temperature, three component winds, major composition). These results provide confidence in the validity of the global thermospheric circulation pattern for mean conditions.

4.1. Nightside Temperature

The first key observation is the nightside warm layer, which was first measured using stellar occultations from SPICAV [*Bertaux et al.*, 2007]. These limited VEx measurements show temperatures of $\sim$185 K up to $\sim$240 K for an altitude range of 95-100 km. These authors state that continued measurements are needed to establish a climatology of these temperatures and confirm a mean value in this nightside altitude region. VEx observations are being supplemented with ground-based observations which generally reveal $\sim$95 to 100 km nightside temperatures near midnight that are cooler ($\sim$160 - 200 K) than the SPICAV values [*Rengel et al.*, 2008; *Clancy et al.*, 2008; *Bailey et al.*, 2008]. See Table 5 for a summary of recent observations of this nightside warm layer.

The VTGCM "mean" simulation (e.g. Figure 6) shows a peak nightside temperature of 188 K at 103 km for comparison with previously discussed observations. This nightside peak temperature, absent in the earlier version of the VTGCM, is directly connected with a more realistic 4.3 micron heating on the dayside, and the resultant enhancement of day-to-night winds. The stronger winds create a larger thermal advection and result in increased adiabatic heating near midnight. The opposite effect on the temperature occurs when the winds are weakened (see section 3.3.2). The VTGCM nightside temperature of $\sim$190 K near 100 km corresponds to an

average case for solar minimum conditions, in accord with available spacecraft and ground-based observations (see Table 5). Continued monitoring will provide additional observations that will help confirm average nightside temperatures.

4.2. O_2 IR Nightside Airglow

The second key observation is the O_2 IR nightside airglow. *Gérard et al.* [2008b] created a statistical hemispheric mean map of the nadir viewed O_2 IR night airglow intensity which provided a maximum emission of $\sim$3 MR, but was later corrected to be $\sim$1.6 MR [*Soret et al.*, 2011]. The peak emission is located near the equator at midnight, but significant variability is shown in the distribution and intensity. In addition, *Piccioni et al.* [2009] created a similar O_2 IR nightglow map using an expanded data set that overlaps the one used by *Gérard et al.* [2008b] for their map. The maximum vertical emission rate is 1.2 MR and is located at the antisolar point slightly below the equator. The *Soret et al.* [2011] O_2 IR nightglow map illustrated a hemispheric average intensity of $\sim$0.5 MR, while *Piccioni et al.* [2009] calculated a mean total vertical emission rate of 0.52 MR. *Gérard et al.* [2009a] and *Soret et al.* [2011] have been able to deduce nightside O density profiles (consistent with O_2 IR nightglow maps) which provide additional valuable constraints for modelers.

The *Gérard et al.* [2008b] one-dimensional chemical diffusive model can replicate the O_2 IR night airglow peak altitude. This nightside one-dimensional model has two main tunable parameters: the downward flux of atomic oxygen and the eddy diffusion coefficient. Using these parameters, the authors were able to match the observed O_2 IR night airglow limb profiles. Specifically when modeling the O_2 IR night airglow, they keep the atomic oxygen downward flux at 130 km relatively constant near 3.5 x 10^{12} cm^{-2} s^{-1} and vary the eddy diffusion coefficient (A = 4 x 10^{12}). *Gérard et al.* [2008b] show one of their selected 1-D model fits for a single

orbit. The O density peak obtained when nearly matching the night airglow layer is 1.8 x 10^{11} cm^{-3} at 104 km.

The new VTGCM model produces O_2 nightglow intensities and O density values within the ranges stated in *Gérard et al.* [2008b] and *Gérard et al.* [2009a], and is in excellent accord with mean values derived in those studies. The VTGCM nightside O density peaks at 104 km, compared to VEx mean altitude of 102 km [*Soret et al.*, 2009, 2011], with a value of 3.41 x 10^{11} cm^{-3}, compared to the VEx value of 2 x 10^{11} cm^{-3}. The corresponding net dayside column integrated production is 2.34 x 10^{12} cm^{-2} s^{-1}, while the 1-D model uses a flux of 3.5 x 10^{12} cm^{-2} s^{-1}. An earlier estimate was made using a 1-D photochemical-diffusive transport model and a downward flux of oxygen of 5 x 10^{11} cm^{-2} s^{-1}, which corresponds to a limb profile from VEx orbit 76 at 35°N [*Drossart et al.*, 2007]. This flux had an associated A = 2 x 10^{12} and O density peak of 1.3 x 10^{11} cm^{-3} at 100 km [*Drossart et al.*, 2007]. The O_2 nightglow peak volume emission rate produced by the VTGCM is located at $\sim$100 km with an integrated vertical intensity of 1.76 MR, which is located near 00:00 LT. As mentioned earlier, the VTGCM nightglow result is for a yield of 75% in reaction R1; a 100% yield would provide a VTGCM peak vertical intensity of 2.37 MR. Statistically averaged observations reveal the mean peak intensity to be 1.6 MR at 96 km and on average seen at midnight [*Soret et al.*, 2009, 2011; *Gérard et al.*, 2008b]. The VTGCM produces a hemispheric average intensity of 0.51 - 0.63 MR (averged over a limited nightside box) when compared to VEx 0.47 MR [*Soret et al.*, 2011]. For the VTGCM sensitivity test results, we notice the O_2 IR night airglow layer is controlled by two processes. The altitude is mainly controlled by eddy diffusion and the intensity of the nightglow is controlled by the winds. The stronger the winds, the more O is transported from

the dayside to the nightside resulting in a more intense emission with a corresponding depletion of O on the dayside.

4.3. NO UV Nightside Airglow

The third key observation is the NO UV night airglow. *Bougher et al.* [1990] published results for solar minimum simulations from an older version of the VTGCM. The older VTGCM adopted different values for certain parameters and did not include all the updates the new VTGCM has incorporated. A few of the modified parameters are the newly specified eddy diffusion coefficient, the prescribed RSZ wind profile, updated chemical reaction rates, and near-IR heating and 15 μm cooling rates. Nevertheless, comparing case 5a from *Bougher et al.* [1990] to the new VTGCM best case can be insightful. Case 5a produced a dayside N-density of 2.6 x 10^7 cm^{-3} at 135 km with a corresponding nightside peak density of 1.8 x 10^8 cm^{-3} at 112 km. This case produced a net dayside column production of 1.05 x 10^9 cm^{-2} s^{-1}. The nightglow dark disk average was 0.156 kR with a peak intensity of 0.42 kR for the (0,1) δ band only. Recall that this δ band is $\sim$20% of the total spectrum and was calculated in order to be comparable with the typical PVO observations.

VEx global maps of the statistical mean NO UV night airglow structure do not yet exist, unlike the O_2 IR night airglow. However, *Gérard et al.* [2008c] employed their 1-D model to simulate individual NO UV nightglow limb profiles, just as for the O_2 IR night airglow. This study used several values for *A*, the variable prescribed in the calculation for the eddy diffusion coefficient, to reproduce three limb profiles (7.4 x 10^{11}, 4 x 10^{12}, and 0). The downward nitrogen flux at 130 km ranges between 1 x 10^8 cm^{-2} s^{-1} and 4 x 10^9 $cm^{-2}s^{-1}$, but has a typical value of 2 x 10^9 cm^{-2} s^{-1}. For one specific orbit (Orbit 320), the N(^{4}S) nightside density is 2 x 10^8 cm^{-3} at 122 km [*Gérard et al.*, 2008c]. *Cox* [2010] has calculated a hemispheric averaged $\sim$1.2 kR for

all bands (δ and γ bands) and identified the mean altitude for the NO UV night airglow to be 114.8$\pm$5.8 km, but can vary from 95-132 km [*Gérard et al.*, 2008c; *Cox*, 2010].

The new VTGCM simulates a nightside N(^{4}S) density peak value of 1.37 x 10^8 cm^{-3} at 115 km with a peak volume emission rate of 1.23 x 10^3 (photon cm^{-3} s^{-1}) located at 106 km. The corresponding peak nightglow intensity for solar minimum conditions is 1.83 kR for the combined δ and γ bands. This peak intensity is similar to the old VTGCM value (0.42 kR x 5 = 2.1 kR)[*Bougher et al.*, 1990]. The simulated peak nightside N(^{4}S) density value is a nearly a factor of 1.5 times smaller than that of *Bougher et al.* [1990] and *Gérard et al.* [2008c] values (1.37 x 10^8 vs 2 x 10^8 cm^{-3}). Furthermore, the new VTGCM net day column integrated production (1.58 x 10^{10}) is 15 times greater than *Bougher et al.* [1990] and a factor of 8 greater than *Gérard et al.* [2008c]. The simulated peak nightglow altitude ($\sim$106 km) is at the lower end of the established range; i.e. the range for the peak altitude is 95-132 km with a mean of 113 km [*Gérard et al.*, 2008c]. Abel inversion of 725 deconvolved limb profiles [*Cox*, 2010] indicates that the peak volume emission rate is located at 114.8$\pm$5.8 km. The hemispheric averaged intensity on the nightside is 1.2 kR while the new VTGCM simulates a smaller intensity of 0.68 kR, but once again similar to the old VTGCM value [*Bougher et al.*, 1990; *Gérard et al.*, 2008c; *Cox*, 2010]. Reasonable chemical reaction rate tests (i.e. within established measurement error bars) have been conducted to increase the simulated intensity and raise the nightglow emission layer; little variation of these nightglow features has resulted. The simulated NO UV night airglow distribution shows a maximum near 01:00 LT. The NO UV night airglow peak emission is not shifted closer to 02:00 LT because the NO UV emission layer is too close in altitude to the O_2 IR emission layer. The calculated separation of these nightglow layers in altitude is $\sim$7 km and the corresponding RSZ wind change is not dramatic (see Figure 8). If the altitude

separation of these two nightglow layers is increased to 17-20 km, the RSZ wind approaches 30 m s^{-1} in the NO UV nightglow layer. This would provide a greater shift in local time for the NO UV nightglow compared to the O_2 IR nightglow.

5. Conclusions

VEx is continuing to make observations that are contributing to a better understanding of Venus' global dynamics in the middle and upper atmosphere. In particular, the VEx O_2 IR nightglow statistical maps are helping to constrain global models and characterize average conditions that permit SS-AS and RSZ components of the upper atmosphere circulation to be estimated. The construction of a NO UV nightglow statistical map is in progress and will also help constrain dynamics in models in a higher altitude region above the O_2 IR nightglow layer. Variability about these statistically mean conditions can be used to characterize the fluctuations of the SS-AS and RSZ wind components at different altitude levels: 90 km -110 km (O_2), 95 km - 132 km (NO).

The VTGCM model is currently able to provide a self consistent view of Venus' time averaged global dynamics in the middle and upper atmosphere. The VTGCM reproduces a nightside warm spot of 188 K at 103 km, consistent with available ground-based and spacecraft observations showing an average of $\sim$190 K at 100 km. Furthermore, the simulated VTGCM O_2 IR nightglow intensity and altitude is a good representation of mean conditions. However, the simulated NO UV nightglow layer altitude is 8-10 km too low and its peak intensity is located near 01:00 LT. If the NO UV layer is raised to $\sim$115 - 120 km, the layer is then positioned into a stronger RSZ wind regime and the peak emission will be located near 02:00 LT, as observed.

With the VTGCM successfully representing mean VEx observations, sensitivity studies were performed with the two tunable parameters (nightside eddy diffusion coefficient and the wave

drag term). The results of the sensitivity studies imply there are at least two sources of variability (eddy diffusion and the vertical winds) impacting nightside emissions. These two sources do not always impact both night airglow emissions equally. The VTGCM simulations clearly show eddy diffusion dominates the region where O_2 IR nightglow emission peaks and the vertical winds dominate the region where NO UV nightglow peaks, both near midnight. These sensitivity tests reveal why the two nightglow layers would vary independently of each other. The dynamical consequences of the eddy diffusion variability and the vertical wind variability can only be simulated utilizing a multi-dimensional dynamical model. *Gérard et al.* [2009a] measured the O_2 IR and NO UV night airglows simultaneously and did not find a spatial correlation between the two nightglows. They explained this lack of correlation by the two different wind regimes encountered by the separate nightglow layers. In VTGCM simulations, it is crucial to prescribe a very weak RSZ below $\sim$110 km and a rapidly growing RSZ above $\sim$110 km to $\sim$130 km to model the nightglow peak emissions at the observed local times. The VTGCM can demonstrate why this non-correlation exists, provided that the distinct nightglow layers are separated in altitude by at least $\sim$15 km.

Future work will examine in more detail the horizontal and vertical O density distributions on the nightside while replacing the Rayleigh friction scheme with a new gravity wave momentum deposition formulation in the VTGCM. *Soret et al.* [2011] have compiled the VIRTIS observations of the O_2 IR nightglow and derived corresponding O density maps. The density maps can provide a detailed constraint for the VTGCM on the nightside since atomic oxygen is the common reactant between the O_2 IR and NO UV nightglow emissions. This data-model comparison may provide insight into why the NO UV nightglow layer simulated by the VTGCM is low in altitude compared to observations. A gravity wave momentum deposition scheme will

be included to simulate disturbances from the lower atmosphere. Wave-like features have been observed by VEx and are thought to be a main contributor to Venus' atmospheric variability and act as the decelerator/accelerator for the general circulation [e.g. *Markiewicz et al.*, 2007; *Peralta et al.*, 2008; *Sánchez-Lavega et al.*, 2008; *Garcia et al.*, 2009].

Acknowledgments. We thank D. L. Huestis for useful discussions concerning this research. This research was sponsored in part by NASA Planetary Atmospheres grant #NNX08AG18G. Both Bougher and Rafkin acknowledge NASA Venus Express Participating Scientist support. NSF grant #AST-0406650 also sponsored a portion of this research. Computer resources were supplied by the National Center for Atmospheric Research, which is sponsored by the National Science Foundation. Lastly, we thank two reviewers for their detailed and constructive comments.

References

Alexander, M. J. (1992), A mechanism for the Venus thermospheric superrotation, *Geophys. Res. Lett.*, *19*, 2207–2210, doi:10.1029/92GL02110.

Anicich, V. G. (1993), Evaluated Bimolecular Ion-Molecule Gas Phase Kinetics of Positive Ions for Use in Modeling Planetary Atmospheres, Cometary Comae, and Interstellar Clouds, *J. of Phys. Chem. Ref. Data*, *22*, 1469–1569, doi:10.1063/1.555940.

Bailey, J., S. Chamberlain, D. Crisp, and V. S. Meadows (2008), Near infrared imaging spectroscopy of Venus with the Anglo-Australian Telescope, *Planet. Space Sci.*, *56*, 1385–1390, doi:10.1016/j.pss.2008.03.006.

Baulch, D. L., D. Drysdale, D. G. Horne, and A. C. Lloyd (1973), Homogeneous gas phase reactions of the H_2-N_2-O_2 system, in *Evaluated Kinetic Data for High Temperature Reactions*, vol. 2, pp. 1–557, Chemical Rubber Company Press, Cleveland, Ohio.

Baulch, D. L., R. A. Cox, R. F. Hampson, J. A. Kerr, J. Troe, and W. R. T. (1980), Evaluated kinetic and photochemical data for atmospheric chemistry, *J. of Phys. Chem. Ref. Data*, *9*, 295.

Bertaux, J., et al. (2007), A warm layer in Venus' cryosphere and high-altitude measurements of HF, HCl, H_2O and HDO, *Nature*, *450*, 646–649, doi:10.1038/nature05974.

Bougher, S. W., and W. J. Borucki (1994), Venus O_2 visible and IR nightglow: Implications for lower thermosphere dynamics and chemistry, *J. Geophys. Res.*, *99*, 3759–3776, doi:10.1029/93JE03431.

Bougher, S. W., R. E. Dickinson, E. C. Ridley, R. G. Roble, A. F. Nagy, and T. E. Cravens (1986), Venus mesosphere and thermosphere. II - Global circulation, temperature, and density variations, *Icarus*, *68*, 284–312, doi:10.1016/0019-1035(86)90025-4.

Bougher, S. W., R. G. E. Roble, R. E. Dickinson, and E. C. Ridley (1988), Venus mesosphere and thermosphere. III - Three-dimensional general circulation with coupled dynamics and composition, *Icarus*, *73*, 545–573, doi:10.1016/0019-1035(88)90064-4.

Bougher, S. W., J.-C. Gérard, A. I. F. Stewart, and C. G. Fesen (1990), The Venus nitric oxide night airglow - Model calculations based on the Venus Thermospheric General Circulation Model, *J. Geophys. Res.*, *95*, 6271–6284, doi:10.1029/JA095iA05p06271.

Bougher, S. W., D. M. Hunten, and R. G. Roble (1994), CO_2 cooling in terrestrial planet thermospheres, *J. Geophys. Res.*, *99*, 14,609–+, doi:10.1029/94JE01088.

Bougher, S. W., M. J. Alexander, and H. G. Mayr (1997), Upper Atmosphere Dynamics: Global Circulation and Gravity Waves, in *Venus II: Geology, Geophysics, Atmosphere, and Solar Wind Environment*, edited by S. W. Bougher, D. M. Hunten, & R. J. Phillips, pp. 259 –291.

Bougher, S. W., S. Engel, R. G. Roble, and B. Foster (1999), Comparative terrestrial planet thermospheres 2. Solar cycle variation of global structure and winds at equinox, *J. Geophys. Res.*, *104*, 16,591–16,611, doi:10.1029/1998JE001019.

Bougher, S. W., R. G. Roble, and T. Fuller-Rowell (2002), Simulations of the Upper Atmospheres of the Terrestrial Planets, in *Atmospheres in the Solar System: Comparative Aeronomy; AGU Geophysical Monogragh 130*, edited by Mendillo, M., Nagy, A., & Waite, J. H., pp. 261–288.

Bougher, S. W., S. Rafkin, and P. Drossart (2006), Dynamics of the Venus upper atmosphere: Outstanding problems and new constraints expected from Venus Express, *Planet. Space Sci.*, *54*, 1371–1380, doi:10.1016/j.pss.2006.04.023.

Bougher, S. W., P. Blelly, M. Combi, J. L. Fox, I. Mueller-Wodarg, A. Ridley, and R. G. Roble (2008), Neutral Upper Atmosphere and Ionosphere Modeling, *Space Science Reviews*, *139*,

107–141, doi:10.1007/s11214-008-9401-9.

Brecht, A., S. Bougher, S. Rafkin, and B. Foster (2007), Venus Upper Atmosphere Winds Traced by Night Airglow Distributions: NCAR VTGCM Simulations, paper presented at AGU Fall Meeting, San Francisco, CA, USA, b1299.

Brecht, A., S. W. Bougher, C. D. Parkinson, Y. L. Yung, and S. C. Rafkin (2009), Understanding the Variability of Nightside Temperatures and Airglow Emissions in Venus' Middle and Upper Atmosphere: NCAR VTGCM Simulations, paper presented at AGU Fall Meeting, San Francisco, CA, USA, a1267.

Campbell, I. M., and C. N. Gray (1973), Rate constants for O(^{3}P) recombination and association with N(^{4}S), *Chemical Physics Letters*, *18*, 607–609, doi:10.1016/0009-2614(73)80479-8.

Campbell, I. M., and B. A. Thrush (1966), Behaviour of carbon dioxide and nitrous oxide in active nitrogen, *Trans. Faraday Soc.*, *62*, 3366–3374.

Clancy, R. T., and D. O. Muhleman (1991), Long-term (1979-1990) changes in the thermal, dynamical, and compositional structure of the Venus mesosphere as inferred from microwave spectral line observations of ^{12}CO, ^{13}CO, and C^{18}O, *Icarus*, *89*, 129–146, doi:10.1016/0019-1035(91)90093-9.

Clancy, R. T., B. J. Sandor, and G. H. Moriarty-Schieven (2003), Observational definition of the Venus mesopause: vertical structure, diurnal variation, and temporal instability, *Icarus*, *161*, 1–16, doi:10.1016/S0019-1035(02)00022-2.

Clancy, R. T., B. J. Sandor, and G. H. Moriarty-Schieven (2008), Venus upper atmospheric CO, temperature, and winds across the afternoon/evening terminator from June 2007 JCMT sub-millimeter line observations, *Planet. Space Sci.*, *56*, 1344–1354, doi:10.1016/j.pss.2008.05.007.

Collet, A., C. Cox, and J. C. Gérard (2010), Two-dimensional time-dependent model of the transport of minor species in the Venus night side upper atmosphere, *Planet. Space Sci.*, doi: 10.1016/j.pss.2010.08.016 in press.

Connes, P., J. F. Noxon, W. A. Traub, and N. P. Carleton (1979), $O_2(^1\ \Delta)$ emission in the day and night airglow of Venus, *Astrophys. J.*, *233*, L29–L32, doi:10.1086/183070.

Cox, C. (2010), Analyse et modélisation des émissions ultraviolettes de l'atmosphère de Vénus et de Mars à l'aide des instruments SPICAM et SPICAV, Ph.D. thesis, Université de Liège.

Crisp, D., V. S. Meadows, B. Bézard, C. de Bergh, J. Maillard, and F. P. Mills (1996), Ground-based near-infrared observations of the Venus nightside: 1.27-μm $O_2(a\Delta_g)$ airglow from the upper atmosphere, *J. Geophys. Res.*, *101*, 4577–4594, doi:10.1029/95JE03136.

Dalgarno, A., J. F. Babb, and Y. Sun (1992), Radiative association in planetary atmospheres, *Planet. Space Sci.*, *40*, 243–246, doi:10.1016/0032-0633(92)90062-S.

Deming, D., and M. J. Mumma (1983), Modeling of the 10-micron natural laser emission from the mesospheres of Mars and Venus, *Icarus*, *55*, 356–368, doi:10.1016/0019-1035(83)90108-2.

Dickinson, R. E. (1972), Infrared radiative heating and cooling in the Venusian mesosphere. I. Global mean radiative equilibrium., *Journal of Atmospheric Sciences*, *29*, 1531–1556, doi: 10.1175/1520-0469(1972)029<1531:IRHACI>2.0.CO;2.

Dickinson, R. E., and S. W. Bougher (1986), Venus mesosphere and thermosphere. I - Heat budget and thermal structure, *J. Geophys. Res.*, *91*, 70–80, doi:10.1029/JA091iA01p00070.

Dickinson, R. E., and E. C. Ridley (1972), Numerical solution for the composition of a thermosphere in the presence of a steady subsolar to-antisolar circulation with application to venus, *Journal of the Atmospheric Sciences*, *29*(8), 1557–1570, doi:10.1175/1520-

0469(1972)029<1557:NSFTCO>2.0.CO;2.

Dickinson, R. E., and E. C. Ridley (1977), Venus mesosphere and thermosphere temperature structure. II - Day-night variations, *Icarus*, *30*, 163–178, doi:10.1016/0019-1035(77)90130-0.

Drossart, P., et al. (2007), A dynamic upper atmosphere of Venus as revealed by VIRTIS on Venus Express, *Nature*, *450*, 641–645, doi:10.1038/nature06140.

Fehsenfeld, F. C., D. B. Dunkin, and E. E. Ferguson (1970), Rate constants for the reaction of CO_2^+ with O, O_2 and NO; N_2^+ with O and NO; and O_2^+ with NO, *Planet. Space Sci.*, *18*, 1267–1269, doi:10.1016/0032-0633(70)90216-3.

Feldman, P. D., H. W. Moos, J. T. Clarke, and A. L. Lane (1979), Identification of the UV nightglow from Venus, *Nature*, *279*, doi:10.1038/279221a0.

Fox, J. L. (1988), Heating efficiencies in the thermosphere of Venus reconsidered, *Planet. Space Sci.*, *36*, 37–46, doi:10.1016/0032-0633(88)90144-4.

Fox, J. L. (1994), Rate coefficient for the reaction N + NO, *J. Geophys. Res.*, *99*, 6273–6276, doi:10.1029/93JA03299.

Fox, J. L., and K. Y. Sung (2001), Solar activity variations of the Venus thermosphere/ionosphere, *J. Geophys. Res.*, *106*, 21,305–21,336, doi:10.1029/2001JA000069.

Fox, J. L., M. I. Galand, and R. E. Johnson (2008), Energy Deposition in Planetary Atmospheres by Charged Particles and Solar Photons, *Space Science Reviews*, *139*, 3–62, doi:10.1007/s11214-008-9403-7.

Garcia, R. F., P. Drossart, G. Piccioni, M. López-Valverde, and G. Occhipinti (2009), Gravity waves in the upper atmosphere of Venus revealed by CO_2 nonlocal thermodynamic equilibrium emissions, *J. Geophys. Res. (Planets)*, *114*(E00B32), doi:10.1029/2008JE003073.

Gérard, J., B. Hubert, V. I. Shematovich, D. V. Bisikalo, and G. R. Gladstone (2008a), The Venus ultraviolet oxygen dayglow and aurora: Model comparison with observations, *Planet. Space Sci.*, *56*, 542–552, doi:10.1016/j.pss.2007.11.008.

Gérard, J. C., A. I. F. Stewart, and S. W. Bougher (1981), The altitude distribution of the Venus ultraviolet nightglow and implications on vertical transport, *Geophys. Res. Lett.*, *8*, 633–636, doi:10.1029/GL008i006p00633.

Gérard, J. C., A. Saglam, G. Piccioni, P. Drossart, C. Cox, S. Erard, R. Hueso, and A. Sánchez-Lavega (2008b), Distribution of the O_2 infrared nightglow observed with VIRTIS on board Venus Express, *Geophys. Res. Lett.*, *35*, doi:10.1029/2007GL032021.

Gérard, J. C., C. Cox, A. Saglam, J. Bertaux, E. Villard, and C. Nehmé (2008c), Limb observations of the ultraviolet nitric oxide nightglow with SPICAV on board Venus Express, *J. Geophys. Res. (Planets)*, *113*(E12), doi:10.1029/2008JE003078.

Gérard, J. C., A. Saglam, G. Piccioni, P. Drossart, F. Montmessin, and J. Bertaux (2009a), Atomic oxygen distribution in the Venus mesosphere from observations of O_2 infrared airglow by VIRTIS-Venus Express, *Icarus*, *199*, 264–272, doi:10.1016/j.icarus.2008.09.016.

Gérard, J. C., C. Cox, L. Soret, A. Saglam, G. Piccioni, J. Bertaux, and P. Drossart (2009b), Concurrent observations of the ultraviolet nitric oxide and infrared O_2 nightglow emissions with Venus Express, *J. Geophys. Res. (Planets)*, *114*(E00B44), doi:10.1029/2009JE003371.

Gérard, J. C., L. Soret, A. Saglam, G. Piccioni, and P. Drossart (2010), The distributions of the OH Meinel and $O_2(a^1\Delta - X^3\Sigma)$ nightglow emissions in the Venus mesosphere based on VIRTIS observations, *Advances in Space Research*, *45*, 1268–1275, doi:10.1016/j.asr.2010.01.022.

Gilli, G., M. A. López-Valverde, P. Drossart, G. Piccioni, S. Erard, and A. Cardesín Moinelo

(2009), Limb observations of CO_2 and CO non-LTE emissions in the Venus atmosphere by VIRTIS/Venus Express, *J. Geophys. Res. (Planets)*, *114*, doi:10.1029/2008JE003112.

Goldstein, J. J., M. J. Mumma, T. Kostiuk, D. Deming, F. Espenak, and D. Zipoy (1991), Absolute wind velocities in the lower thermosphere of Venus using infrared heterodyne spectroscopy, *Icarus*, *94*, 45–63, doi:10.1016/0019-1035(91)90140-O.

Gordiets, B. F., and V. I. Panchenko (1983), Nonequilibrium infrared emission and the natural laser effect in the Venus and Mars atmospheres, *Cosmic Research*, *21*, 725–734.

Gougousi, T. (1997), Electron-ion recombination rate coefficient measurements in a flowing afterglow plasma, *Chem. Phys. Lett.*, *265*, 399–403, doi:10.1016/S0009-2614(96)01488-1.

Hampson, R. F., Jr. (1980), Chemical kinetic and Photochemical Data Sheets for Atmospheric Reactions. Report No. FAA-EE-80-17, U.S. Dept. of Transportation, FAA Office of Environment and Energy, High Altitude Pollution Program, Washington, D.C.

Hedin, A. E., H. B. Niemann, W. T. Kasprzak, and A. Seiff (1983), Global empirical model of the Venus thermosphere, *J. Geophys. Res.*, *88*, 73–83, doi:10.1029/JA088iA01p00073.

Herron, J. (1999), Evaluated Chemical Kinetics Data for Reactions of $N(^2D)$ $N(^2P)$, and $N_2(A^3\Sigma_u^+)$ in the Gas Phase, *J. of Phys. Chem. Ref. Data*, *28*, 1453–1483, doi: 10.1063/1.556043.

Hierl, P. M., I. Dotan, J. V. Seeley, J. M. van Doren, R. A. Morris, and A. A. Viggiano (1997), Rate constants for the reactions of O^+ with N_2 and O_2 as a function of temperature (300-1800 K), *J. Chem. Phys.*, *106*, 3540–3544, doi:10.1063/1.473450.

Hueso, R., A. Sánchez-Lavega, G. Piccioni, P. Drossart, J. C. Gérard, I. Khatuntsev, L. Zasova, and A. Migliorini (2008), Morphology and dynamics of Venus oxygen airglow from Venus Express/Visible and Infrared Thermal Imaging Spectrometer observations, *J. Geophys. Res.*

(Planets), *113*(E12), doi:10.1029/2008JE003081.

Huestis, D. L. (2002), Current Laboratory Experiments for Planetary Aeronomy, in *Atmospheres in the Solar System: Comparative Aeronomy*, edited by Mendillo, M., Nagy, A., & Waite, J. H., p. 245.

Jamieson, C., R. M. Garcia, D. A. Pejakovic, and K. S. Kalogerakis (2009a), Oxygen Atom Recombination in Carbon Dioxide Atmospheres, in *AAS/Division for Planetary Sciences Meeting Abstracts*, *AAS/Division for Planetary Sciences Meeting Abstracts*, vol. 41, p. 54.01.

Jamieson, C. S., R. M. Garcia, D. Pejakovic, and K. Kalogerakis (2009b), The Kinetics of Oxygen Atom Recombination in the Presence of Carbon Dioxide, paper presented at AGU Fall Meeting, San Francisco, CA, USA, d1156.

Kasprzak, W. T., A. E. Hedin, H. G. Mayr, and H. B. Niemann (1988), Wavelike perturbations observed in the neutral thermosphere of Venus, *J. Geophys. Res.*, *93*, 11,237–11,245, doi: 10.1029/JA093iA10p11237.

Kasprzak, W. T., H. B. Niemann, A. E. Hedin, S. W. Bougher, and D. M. Hunten (1993), Neutral composition measurements by the Pioneer Venus Neutral Mass Spectrometer during Orbiter re-entry, *Geophys. Res. Lett.*, *20*, 2747–2750, doi:10.1029/93GL02241.

Kasprzak, W. T., G. M. Keating, N. C. Hsu, A. I. F. Stewart, W. B. Colwell, and S. W. Bougher (1997), Solar Activity Behavior of the Thermosphere, in *Venus II: Geology, Geophysics, Atmosphere, and Solar Wind Environment*, edited by S. W. Bougher, D. M. Hunten, & R. J. Phillips.

Keating, G. M., F. W. Taylor, J. Y. Nicholson, and E. W. Hinson (1979), Short-term cyclic variations and diurnal variations of the Venus upper atmosphere, *Science*, *205*, 62–64, doi: 10.1126/science.205.4401.62.

Keating, G. M., J. Y. Nicholson, and L. R. Lake (1980), Venus upper atmosphere structure, *J. Geophys. Res.*, *85*, 7941–7956, doi:10.1029/JA085iA13p07941.

Keating, G. M., J. L. Bertaux, S. W. Bougher, R. E. Dickinson, T. E. Cravens, and A. E. Hedin (1985), Models of Venus neutral upper atmosphere - Structure and composition, *Advances in Space Research*, *5*, 117–171, doi:10.1016/0273-1177(85)90200-5.

Krasnopolsky, V. A. (2010), Venus night airglow: Ground-based detection of OH, observations of O_2 emissions, and photochemical model, *Icarus*, *207*, 17–27, doi: 10.1016/j.icarus.2009.10.019.

Lellouch, E., T. Clancy, D. Crisp, A. J. Kliore, D. Titov, and S. W. Bougher (1997), Monitoring of Mesospheric Structure and Dynamics, in *Venus II: Geology, Geophysics, Atmosphere, and Solar Wind Environment*, edited by S. W. Bougher, D. M. Hunten, & R. J. Phillips, pp. 295 – 324.

López-Valverde, M. A., P. Drossart, R. Carlson, R. Mehlman, and M. Roos-Serote (2007), Non-LTE infrared observations at Venus: From NIMS/Galileo to VIRTIS/Venus Express, *Planet. Space Sci.*, *55*, 1757–1771, doi:10.1016/j.pss.2007.01.008.

Maillard, J., E. Lellouch, J. Crovisier, C. de Bergh, and B. Bézard (1995), Carbon Monoxide 4.7 μm Emission: A New Dynamical Probe of Venus' Thermosphere, in *Bulletin of the American Astronomical Society*, *Bulletin of the American Astronomical Society*, vol. 27, p. 1080.

Markiewicz, W. J., D. V. Titov, S. S. Limaye, H. U. Keller, N. Ignatiev, R. Jaumann, N. Thomas, H. Michalik, R. Moissl, and P. Russo (2007), Morphology and dynamics of the upper cloud layer of Venus, *Nature*, *450*, 633–636, doi:10.1038/nature06320.

Massie, S. T., D. M. Hunten, and D. R. Sowell (1983), Day and night models of the Venus thermosphere, *J. Geophys. Res.*, *88*, 3955–3969, doi:10.1029/JA088iA05p03955.

Mehr, F. J., and M. A. Biondi (1969), Electron Temperature Dependence of Recombination of O_2^+ and N_2^+ Ions with Electrons, *Physical Review*, *181*, 264–271, doi: 10.1103/PhysRev.181.264.

Midey, A. J., and A. A. Viggiano (1999), Rate constants for the reaction of O_2^+ with NO from 300 to 1400 K, *J. Chem. Phys.*, *110*, 10,746–10,748, doi:10.1063/1.479017.

Moissl, R., I. Khatuntsev, S. S. Limaye, D. V. Titov, W. J. Markiewicz, N. I. Ignatiev, T. Roatsch, K. Matz, R. Jaumann, M. Almeida, G. Portyankina, T. Behnke, and S. F. Hviid (2009), Venus cloud top winds from tracking UV features in Venus Monitoring Camera images, *J. Geophys. Res. (Planets)*, *114*, E00B31, doi:10.1029/2008JE003117.

Nair, H., M. Allen, A. D. Anbar, Y. L. Yung, and R. T. Clancy (1994), A photochemical model of the martian atmosphere, *Icarus*, *111*, 124–150, doi:10.1006/icar.1994.1137.

Ohtsuki, S., N. Iwagami, H. Sagawa, Y. Kasaba, M. Ueno, and T. Imamura (2005), Ground-based observation of the Venus 1.27-μm O_2 airglow, *Advances in Space Research*, *36*, 2038–2042, doi:10.1016/j.asr.2005.05.078.

Ohtsuki, S., N. Iwagami, H. Sagawa, M. Ueno, Y. Kasaba, T. Imamura, and E. Nishihara (2008), Imaging spectroscopy of the Venus 1.27-μm O_2 airglow with ground-based telescopes, *Advances in Space Research*, *41*, 1375–1380, doi:10.1016/j.asr.2007.10.014.

Pätzold, M., B. Häusler, M. K. Bird, S. Tellmann, R. Mattei, S. W. Asmar, V. Dehant, W. Eidel, T. Imamura, R. A. Simpson, and G. L. Tyler (2007), The structure of Venus' middle atmosphere and ionosphere, *Nature*, *450*, 657–660, doi:10.1038/nature06239.

Peralta, J., R. Hueso, A. Sánchez-Lavega, G. Piccioni, O. Lanciano, and P. Drossart (2008), Characterization of mesoscale gravity waves in the upper and lower clouds of Venus from VEX-VIRTIS images, *J. Geophys. Res. (Planets)*, *113*(E12), doi:10.1029/2008JE003185.

Piccioni, G., P. Drossart, L. Zasova, A. Migliorini, J. Gérard, F. P. Mills, A. Shakun, A. García Muñoz, N. Ignatiev, D. Grassi, V. Cottini, F. W. Taylor, S. Erard, and The Virtis-Venus Express Technical Team (2008), First detection of hydroxyl in the atmosphere of Venus, *Astron. Astrophys.*, *483*, L29–L33, doi:10.1051/0004-6361:200809761.

Piccioni, G., L. Zasova, A. Migliorini, P. Drossart, A. Shakun, A. García Muñoz, F. P. Mills, and A. Cardesin-Moinelo (2009), Near-IR oxygen nightglow observed by VIRTIS in the Venus upper atmosphere, *J. Geophys. Res. (Planets)*, *114*(E00B38), doi:10.1029/2008JE003133.

Rengel, M., P. Hartogh, and C. Jarchow (2008), Mesospheric vertical thermal structure and winds on Venus from HHSMT CO spectral-line observations, *Planet. Space Sci.*, *56*, 1368–1384, doi:10.1016/j.pss.2008.07.004.

Roldán, C., M. A. López-Valverde, M. López-Puertas, and D. P. Edwards (2000), Non-LTE Infrared Emissions of CO_2 in the Atmosphere of Venus, *Icarus*, *147*, 11–25, doi: 10.1006/icar.2000.6432.

Sánchez-Lavega, A., R. Hueso, G. Piccioni, P. Drossart, J. Peralta, S. Pérez-Hoyos, C. F. Wilson, F. W. Taylor, K. H. Baines, D. Luz, S. Erard, and S. Lebonnois (2008), Variable winds on Venus mapped in three dimensions, *Geophys. Res. Lett.*, *35*, L13,204, doi: 10.1029/2008GL033817.

Sander, S. P., et al. (2003), Chemical Kinetics and Photochemical Data for use in Atmospheric Studies, Evaluation No. 14, *JPL Publication 02-25*.

Schofield, J. T., and F. W. Taylor (1983), Measurements of the mean, solar-fixed temperature and cloud structure of the middle atmosphere of Venus, *Quarterly Journal of the Royal Meteorological Society*, *109*, 57–80, doi:10.1256/smsqj.45903.

Schubert, G., C. Covey, A. del Genio, L. S. Elson, G. Keating, A. Seiff, R. E. Young, J. Apt, C. C. Counselman, A. J. Kliore, S. S. Limaye, H. E. Revercomb, L. A. Sromovsky, V. E. Suomi, F. Taylor, R. Woo, and U. von Zahn (1980), Structure and circulation of the Venus atmosphere, *J. Geophys. Res.*, *85*, 8007–8025, doi:10.1029/JA085iA13p08007.

Schubert, G., S. W. Bougher, A. D. Covey, C. C.and Del Genio, A. S. Grossman, J. L. Hollingsworth, S. S. Limaye, and R. E. Young (2007), Venus atmosphere dynamics: A continuing enigma, in *Exploring Venus as terrestrial planet, AGU Geophysical Monograph 176*, edited by L. W. Esposito, E. R. Stofan, & T. E. Cravens, pp. 121–138.

Scott, G. B. I., D. A. Fairley, C. G. Freeman, M. J. McEwan, and V. G. Anicich (1998), Gas-phase reactions of some positive ions with atomic and molecular nitrogen, *J. Chem. Phys.*, *109*, 9010–9014, doi:10.1063/1.477571.

Seiff, A., and D. B. Kirk (1982), Structure of the Venus mesosphere and lower thermosphere from measurements during entry of the Pioneer Venus probes, *Icarus*, *49*, 49–70, doi:10.1016/0019-1035(82)90056-2.

Seiff, A., J. T. Schofield, A. J. Kliore, F. W. Taylor, and S. S. Limaye (1985), Models of the structure of the atmosphere of Venus from the surface to 100 kilometers altitude, *Advances in Space Research*, *5*, 3–58, doi:10.1016/0273-1177(85)90197-8.

Shah, K. P., D. O. Muhleman, and G. L. Berge (1991), Measurement of winds in Venus' upper mesosphere based on Doppler shifts of the 2.6-mm (C-12)O line, *Icarus*, *93*, 96–121, doi: 10.1016/0019-1035(91)90167-R.

Soret, L., J. C. Gérard, A. Saglam, G. Piccioni, and P. Drossart (2009), Latitudinal - local time distribution of the O_2 and OH infrared nightglows and O density in the Venus lower thermosphere, paper presented at European Planetary Science Congress, Potsdam, German,

http://meetings.copernicus.org/epsc2009, p.160.

Soret, L., J. C. Gérard, G. Piccioni, and P. Drossart (2010), Venus OH Nightglow Distribution from VIRTIS Limb Observations from Venus Express, *Geophys. Res. Lett.*, *37*(L06805), doi: 10.1029/2010GL042377.

Soret, L., J. C. Gérard, F. Montmessin, G. Piccioni, P. Drossart, and J.-L. Bertaux (2011), Atomic Oxygen on the Venus Nightside: global distribution deduced from airglow mapping, *Icarus, in press*.

Sornig, M., T. Livengood, G. Sonnabend, P. Kroetz, D. Stupar, T. Kostiuk, and R. Schieder (2008), Venus upper atmosphere winds from ground-based heterodyne spectroscopy of CO_2 at 10μm wavelength, *Planet. Space Sci.*, *56*, 1399–1406, doi:10.1016/j.pss.2008.05.006.

Stepanova, G. I., and G. M. Shved (1985), Radiative Transfer in the 4.3-MICRON CO_2 and 4.7-MICRON CO Bands in the Non-LTE Venus and Mars Atmospheres - Transformation of Absorbed Solar Energy, *Sov. Astron.*, *29*, 528–530.

Stewart, A. I., and C. A. Barth (1979), Ultraviolet night airglow of Venus, *Science*, *205*, 59–62, doi:10.1126/science.205.4401.59.

Stewart, A. I. F., J. Gerard, D. W. Rusch, and S. W. Bougher (1980), Morphology of the Venus ultraviolet night airglow, *J. Geophys. Res.*, *85*, 7861–7870, doi:10.1029/JA085iA13p07861.

Svedhem, H., D. Titov, F. Taylor, and O. Witasse (2009), Venus Express mission, *J. Geophys. Res. (Planets)*, *114*, E00B33, doi:10.1029/2008JE003290.

Vejby-Christensen, L., D. Kella, H. B. Pedersen, and L. H. Andersen (1998), Dissociative recombination of NO^+, *Phys. Rev. A*, *57*, 3627–3634, doi:10.1103/PhysRevA.57.3627.

von Zahn, U., K. H. Fricke, H. Hoffmann, and K. Pelka (1979), Venus - Eddy coefficients in the thermosphere and the inferred helium content of the lower atmosphere, *Geophys. Res. Lett.*,

6, 337–340.

Widemann, T., E. Lellouch, and J. Donati (2008), Venus Doppler winds at cloud tops observed with ESPaDOnS at CFHT, *Planet. Space Sci.*, *56*, 1320–1334, doi:10.1016/j.pss.2008.07.005.

Yung, Y. L., and W. B. Demore (1982), Photochemistry of the stratosphere of Venus - Implications for atmospheric evolution, *Icarus*, *51*, 199–247, doi:10.1016/0019-1035(82)90080-X.

Zasova, L. V., V. I. Moroz, V. M. Linkin, I. V. Khatuntsev, and B. S. Maiorov (2006), Structure of the Venusian atmosphere from surface up to 100 km, *Cosmic Research*, *44*, 364–383, doi: 10.1134/S0010952506040095.

Zhang, S., S. W. Bougher, and M. J. Alexander (1996), The impact of gravity waves on the Venus thermosphere and O_2 IR nightglow, *J. Geophys. Res.*, *101*, 23,195–23,206, doi: 10.1029/96JE02035.

Table 1. Key O_2 IR and NO UV nightglow parameters. Rate coefficients are $cm^3\ s^{-1}$ and three body rate coefficients are $cm^6\ s^{-1}$

	$O + O + CO_2 \rightarrow O_2$(a state)	75% yield	*Gérard et al.* [2008b]
R1	$O + O + CO_2 \rightarrow O_2$(a state)	2.75×10^{-32}	*Campbell and Gray* [1973]
R2	O_2(a state) $+ CO_2 \rightarrow O_2 + CO_2$	2×10^{-20}	*Sander et al.* [2003]
R3	$O + CO + CO_2 \rightarrow 2CO_2$	$6.5 \times 10^{-33} \times \exp(-2180/T_n)$	*Baulch et al.* [1980]
R4	$O + O_2 + CO_2 \rightarrow O_3 + CO_2$	1.35×10^{-33}	*Hampson* [1980]
R5	$CO_2^+ + O \rightarrow O^+ + CO_2$	9.60×10^{-11}	*Fox and Sung* [2001]
R6	$CO_2^+ + O \rightarrow O_2^+ + CO$	1.64×10^{-10}	*Fehsenfeld et al.* [1970]
R7	$O_2^+ + e \rightarrow O + O$	$1.95 \times 10^{-7} \times (300/Te)^{0.7}$	*Mehr and Biondi* [1969]
R8	$CO_2^+ + e \rightarrow CO + O$	$3.5 \times 10^{-7} \times (300/Te)^{0.5}$	*Gougousi* [1997]
R9	$O^+ + CO_2 \rightarrow O_2^+ + CO$	1.10×10^{-09}	*Anicich* [1993]
	f	0.5 branching ratio	*Bougher et al.* [1990]
	g	0.75 branching ratio	*Bougher et al.* [1990]
R10	$N(^2D) + CO_2 \rightarrow NO + CO$	2.8×10^{-13}	*Bougher et al.* [1990]
R11	$N(^2D) + O \rightarrow N(^4S) + O$	2.0×10^{-11}	*Bougher et al.* [1990]
R12	$N(^2D) + CO \rightarrow N(^4S) + CO$	1.9×10^{-12}	*Herron* [1999]
R13	$N(^2D) + N_2 \rightarrow N(^4S) + N_2$	1.7×10^{-14}	*Herron* [1999]
R14	$N(^4S) + O_2^+ \rightarrow NO^+ + O$	1.00×10^{-10}	*Scott et al.* [1998]
R15	$N(^4S) + NO \rightarrow N_2 + O$	$2.5 \times 10^{-10} (T_n/300)^{0.5} \exp(-600/T_n)$	*Fox* [1994]
R16	$N(^4S) + O \rightarrow NO^* + h\nu$	$1.9 \times 10^{-17} (300/T_n)^{0.5} (1-0.57/T_n{}^{0.5})$	*Dalgarno et al.* [1992]
R17	$N(^4S) + O + CO_2 \rightarrow NO + CO_2$	$1.83 \times 10^{-32} (298/T_n)^{0.5}$	*Campbell and Thrush* [1966]
R18	$N_2 + O^+ \rightarrow NO^+ + N$	$1.2 \times 10^{-12} (300/T_n)^{0.45}$	*Hierl et al.* [1997]
R19	$NO + O_2^+ \rightarrow NO^+ + O_2$	4.50×10^{-10}	*Midey and Viggiano* [1999]
R20	$NO^+ + e \rightarrow g\ N(^2D) + (1-g)\ N(^4S)$	$4.0 \times 10^{-7} (300/Te)^{0.5}$	*Vejby-Christensen et al.* [1998]
RK1	$CO_2 + h\nu \rightarrow CO + O$		Computed in the VTGCM
RK2	$O_2 + h\nu \rightarrow O + O$		Computed in the VTGCM
RK3	$N_2 + h\nu \rightarrow (1-f)\ N(^4S) + f\ N(^2D)$		Computed in the VTGCM

Table 2. Key Chemical Reaction Rate Tests ($cm^6\ s^{-1}$)

	R1 (O + O + M)	R17 (N + O + M)
Standard	2.75 x 10^{-32} (*Campbell and Gray* [1973])	1.83 x 10^{-32} $(298/T_n)^{0.5}$ (*Campbell and Thrush* [1966])
Test	1.8 x 10^{-32} (*Jamieson et al.* [2009b])	1.1 x 10^{-32} $(300/T_n)^{0.5}$ (*Stewart and Barth* [1979])

Table 3. Results from the Nightside Eddy Diffusion sensitivity test

O_2 (IR)	O Den Peak (Night) (#/cm^3)	Alt. (km)	Peak Intensity (MR)	Nightglow Peak Alt. (km)
Best	3.41 x 10^{11}	104	1.76	100
Max	2.62 x 10^{11}	102	1.04	100
Min	3.93 x 10^{11}	105	2.58	103
NO (UV)	N Den Peak (Night) (#/cm^3)	Alt. (km)	Peak Intensity (kR)	Nightglow Peak Alt. (km)
Best	1.37 x 10^8	115	1.83	106
Max	1.76 x 10^8	109	1.64	104
Min	1.65 x 10^8	118	2.04	109

Table 4. Results from the wind sensitivity test

O_2 (IR)	O Den Peak (Day) (#/cm^3)	Alt. (km)	O Den Peak (Night) (#/cm^3)	Alt. (km)	Peak Intensity (MR)	Nightglow Peak Alt. (km)
Best	5.47 x 10^{10}	94	3.41 x 10^{11}	104	1.76	100
Max	5.56 x 10^{10}	95	2.36 x 10^{11}	104	0.92	99
Min	5.44 x 10^{10}	94	3.93 x 10^{11}	104	2.42	101
NO (UV)	N Den Peak (Day) (#/cm^3)	Alt. (km)	N Den Peak (Night) (#/cm^3)	Alt. (km)	Peak Intensity (kR)	Nightglow Peak Alt. (km)
Best	1.03 x 10^8	136	1.37 x 10^8	115	1.83	106
Max	2.17 x 10^8	134	2.30 x 10^8	115	1.64	110
Min	7.00 x 10^7	136	1.65 x 10^8	115	3.56	106

T_{night}	Peak Temp [K]	Alt. [km]
Best	188	103
Max	173	94
Min	207	105

Table 5. Summary of temperature measurements for the Venus nightside near 95 km from *Bailey et al.* [2008]

Method	Temperature (K)	Reference
1.27 μm O_2 airglow	185 ± 15	*Connes et al.* [1979]
Pioneer Venus night probe deceleration	167.2	*Seiff and Kirk* [1982]
Pioneer Venus OIR	170 - 175	*Schofield and Taylor* [1983]
VIRA (based on OIR and probe deceleration)	168	*Seiff et al.* [1985]
CO mm lines	165 - 210	*Clancy and Muhleman* [1991]
1.27 μm O_2 airglow	186 ± 6	*Crisp et al.* [1996]
CO mm lines	165 - 178	*Clancy et al.* [2003]
1.27 μm O_2 airglow	193 ± 9	*Ohtsuki et al.* [2005]
Venera 15 IR Fourier spectrometer	166.4	*Zasova et al.* [2006]
SPICAV Stellar occultation	194 - 240	*Bertaux et al.* [2007]
Sub-millimeter observations with HHSMT	$\sim$160 - 200	*Rengel et al.* [2008]
Sub-millimeter observations with JCMT	$\sim$175 - 180	*Clancy et al.* [2008]
1.27 μm O_2 airglow (intensity weighted mean)	181 - 196	*Bailey et al.* [2008]

Figure 1. A cartoon of the Venus circulation patterns. The illustration is looking down at the north pole. MT is the morning terminator, ET is the evening terminator, SS-AS is the subsolar-antisolar wind pattern, RSZ is the retrograde superrotating zonal wind pattern. Adopted from *Schubert et al.* [2007].

Figure 2. VTGCM simplified dayside odd oxygen chemical scheme. This provides the sources for atomic O which is transported to the nightside to produce the O_2 IR and NO UV night airglow emissions.

Figure 3. VTGCM simplified dayside odd nitrogen chemical scheme. Taken from *Bougher et al.* [1990].

Figure 4. VTGCM "mean" case for VEx conditions; longitude-height cross section at 2.5°N (local time vs height) for temperature (K).

Figure 5. The heating and cooling terms at LT = 12:00 (A) and LT = 24:00 (B) near the equator. The hashed lines represent cooling and the solid lines represent heating.

Figure 6. VTGCM "mean" case profiles at 2.5°N: (A) temperature (K) at 00:00 LT and (B) total dynamical heating rate (K/day) (adiabatic + total advection) at 00:00 LT.

Figure 7. VTGCM "mean" case for VEx conditions; longitude-height cross section at 2.5°N (local time vs height) for zonal winds (m s^{-1}).

Figure 8. VTGCM "mean" case for VEx conditions; longitude-height cross section at 2.5°N: (A) the morning terminator (MT) (LT = 06:00) total zonal winds (m s^{-1}) where the solid line represents the asymmetric case and the dashed line represents the symmetric case, (B) the evening terminator (ET) (LT = 18:00) total zonal winds (m s^{-1}) where the solid line represents the asymmetric case and the dashed line represents the symmetric case, and (C) the retrograde zonal winds (RSZ) prescribed as a function with height (m s^{-1}).

Figure 9. VTGCM "mean" case for VEx conditions; mixing ratio profiles at 2.5°N (density vs log pressure and height) represented in black and the empirical VTS3 model is represented in red. Top: LT = 12:00 for O, CO, and CO_2. Bottom: LT = 00:00 for O, CO, and CO_2.

Figure 10. VTGCM "mean" case for VEx conditions; density profiles at 2.5°N for atomic oxygen at noon and midnight (left: density vs log pressure vertical scale; right: density vs altitude vertical scale). The density is in units of cm^{-3}.

Figure 11. VTGCM "mean" case for VEx conditions; density profiles at 2.5°N for N(^{4}S) at noon and midnight (left: density vs log pressure vertical scale; right: density vs altitude vertical scale). The density is in units of cm^{-3}.

Figure 12. VTGCM "mean" case for VEx conditions; longitude-height cross section at 2.5°N (local time vs height) illustrates a maximum O_2 IR night airglow volume emission rate close to midnight. The emission rate unit is $\log_{10}$(photons cm^{-3} s^{-1}).

Figure 13. VTGCM "mean" case for VEx conditions; longitude-height cross section at 2.5°N (local time vs height) illustrates a maximum NO UV night airglow volume emission rate close to 01:00 LT. The emission rate unit is $\log_{10}$(photons cm^{-3} s^{-1}).

Figure 14. VTGCM "mean" case for VEx conditions; time scale profiles at 2.5°N (time (day) vs height (km)) for midnight.

Figure 15. VTGCM sensitivity case parameters. (A) The three profiles for the nightside eddy diffusion sensitivity tests. (B) The three resulting evening terminator (LT = 18:00) zonal wind profiles for the wind sensitivity tests.

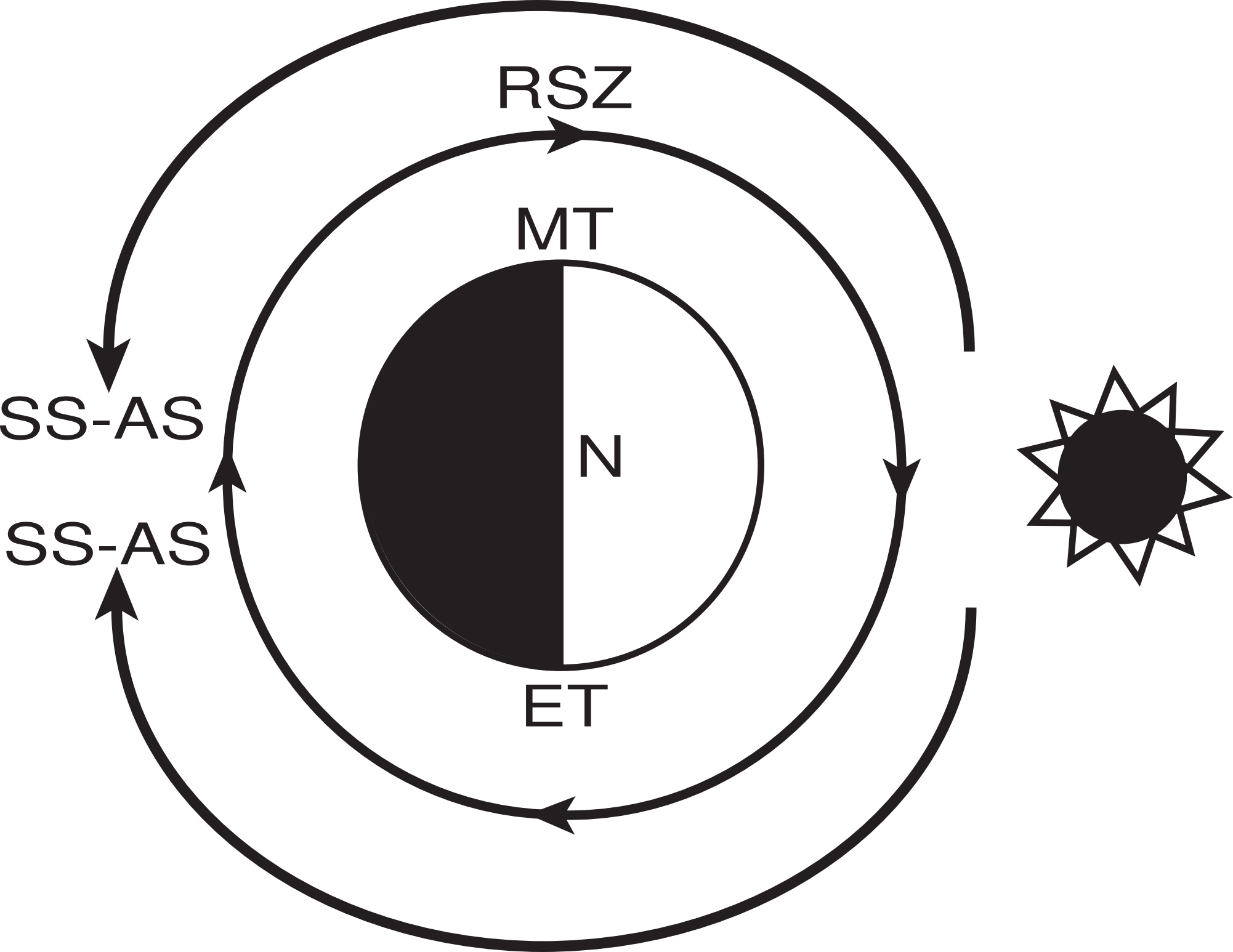
RSZ
MT
SS-AS
N
SS-AS
ET

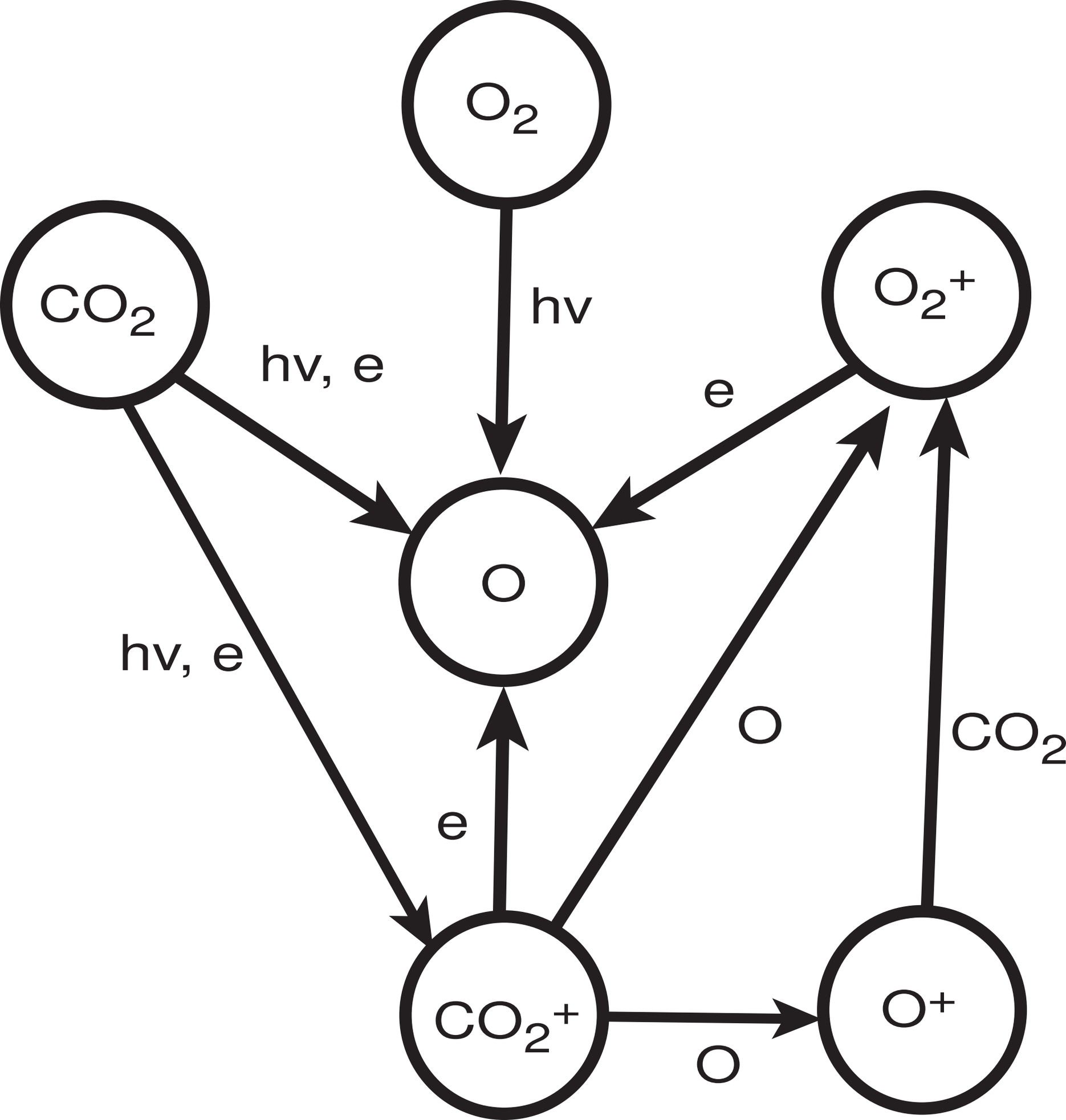
O_2
CO_2
hv
O_2^+
hv, e
e
O
hv, e
O
CO_2
e
CO_2^+
O^+
O

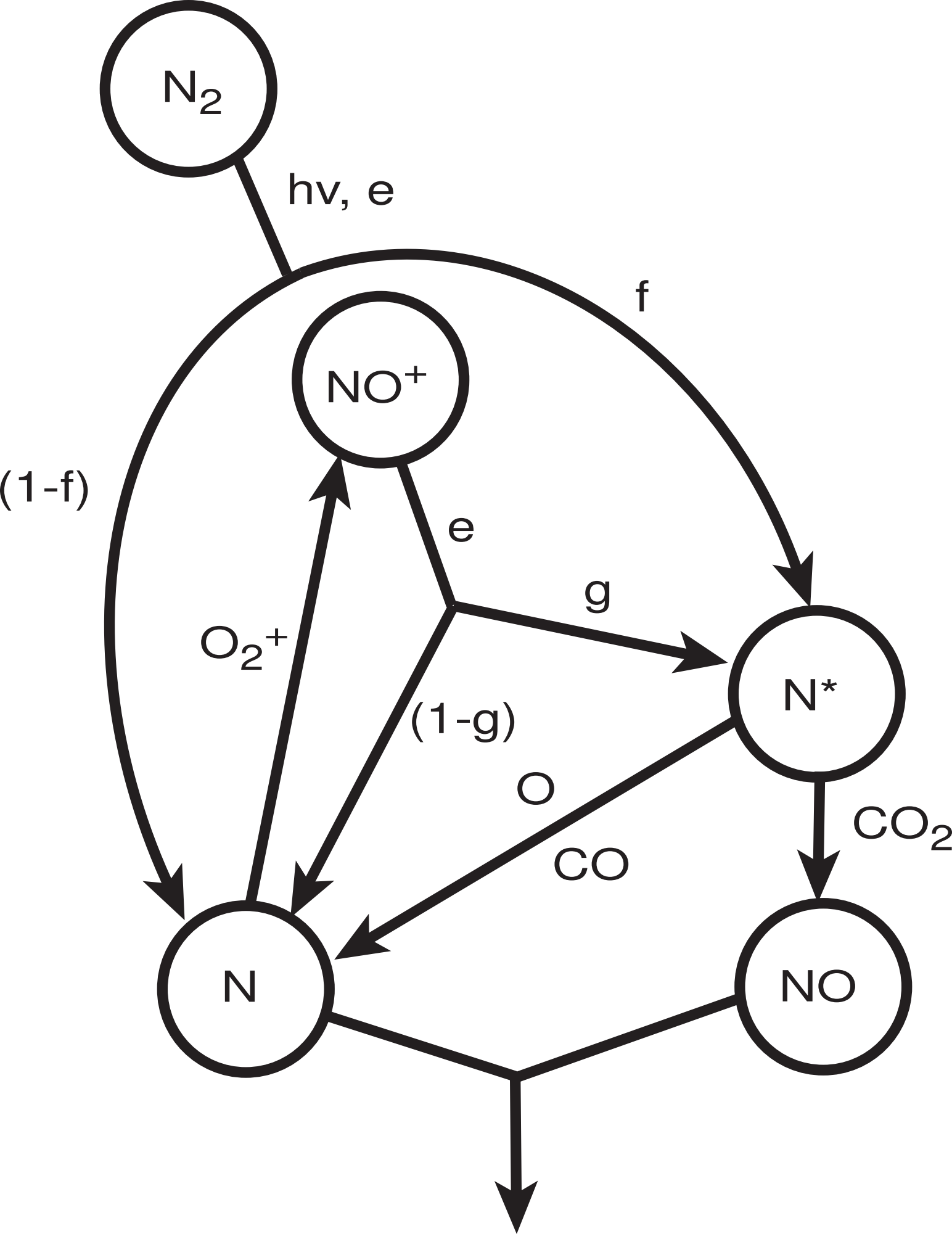
N_2
hv, e
f
NO^+
(1-f)
e
g
O_2^+
(1-g)
N*
O
CO
CO_2
N
NO

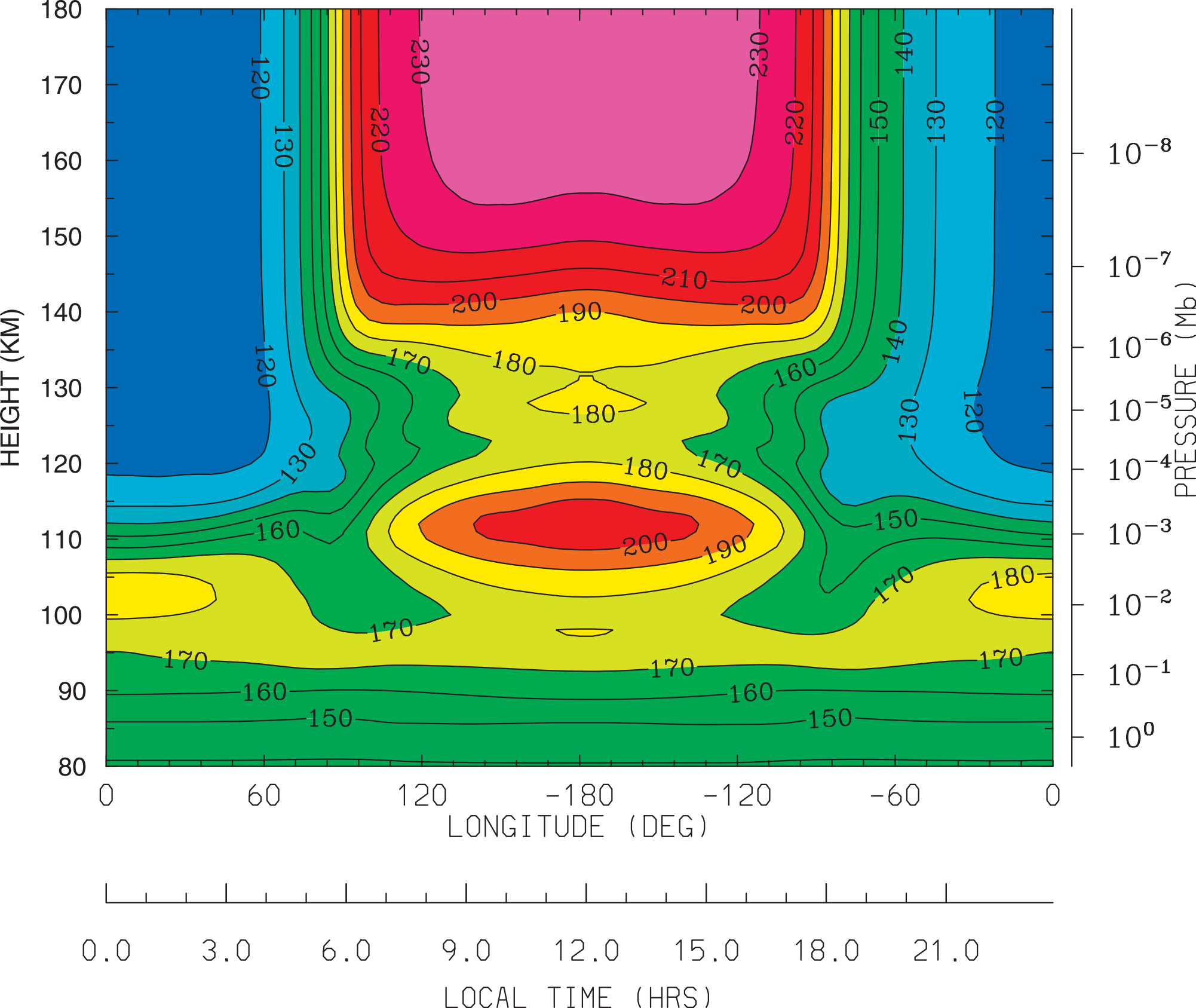
HEIGHT (KM)
180
170
160
150
140
130
120
110
100
90
80
PRESSURE (Mb)
10^{-8}
10^{-7}
10^{-6}
10^{-5}
10^{-4}
10^{-3}
10^{-2}
10^{-1}
10^{0}
0
60
120
-180
-120
-60
0
LONGITUDE (DEG)
0.0
3.0
6.0
9.0
12.0
15.0
18.0
21.0
LOCAL TIME (HRS)

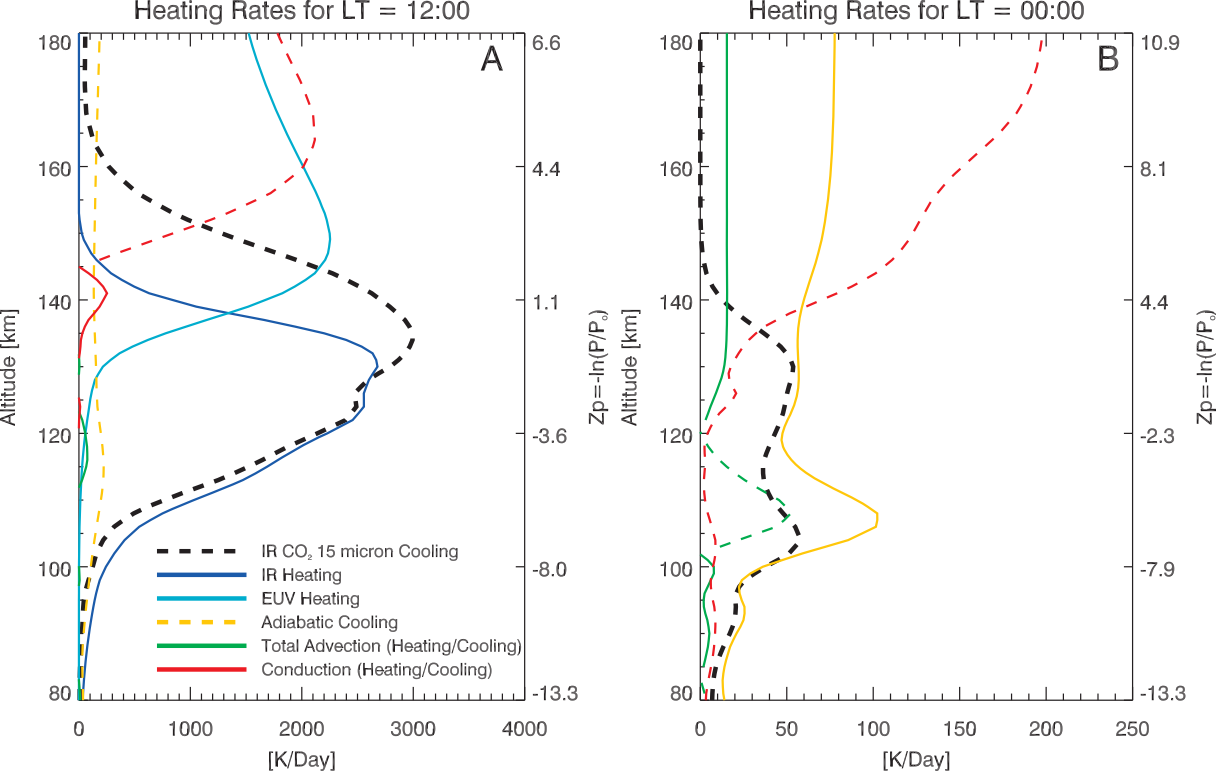
Heating Rates for LT = 12:00
A
Heating Rates for LT = 00:00
B
Altitude [km]
Zp=-ln(P/P∘)
[K/Day]
IR CO2 15 micron Cooling
IR Heating
EUV Heating
Adiabatic Cooling
Total Advection (Heating/Cooling)
Conduction (Heating/Cooling)

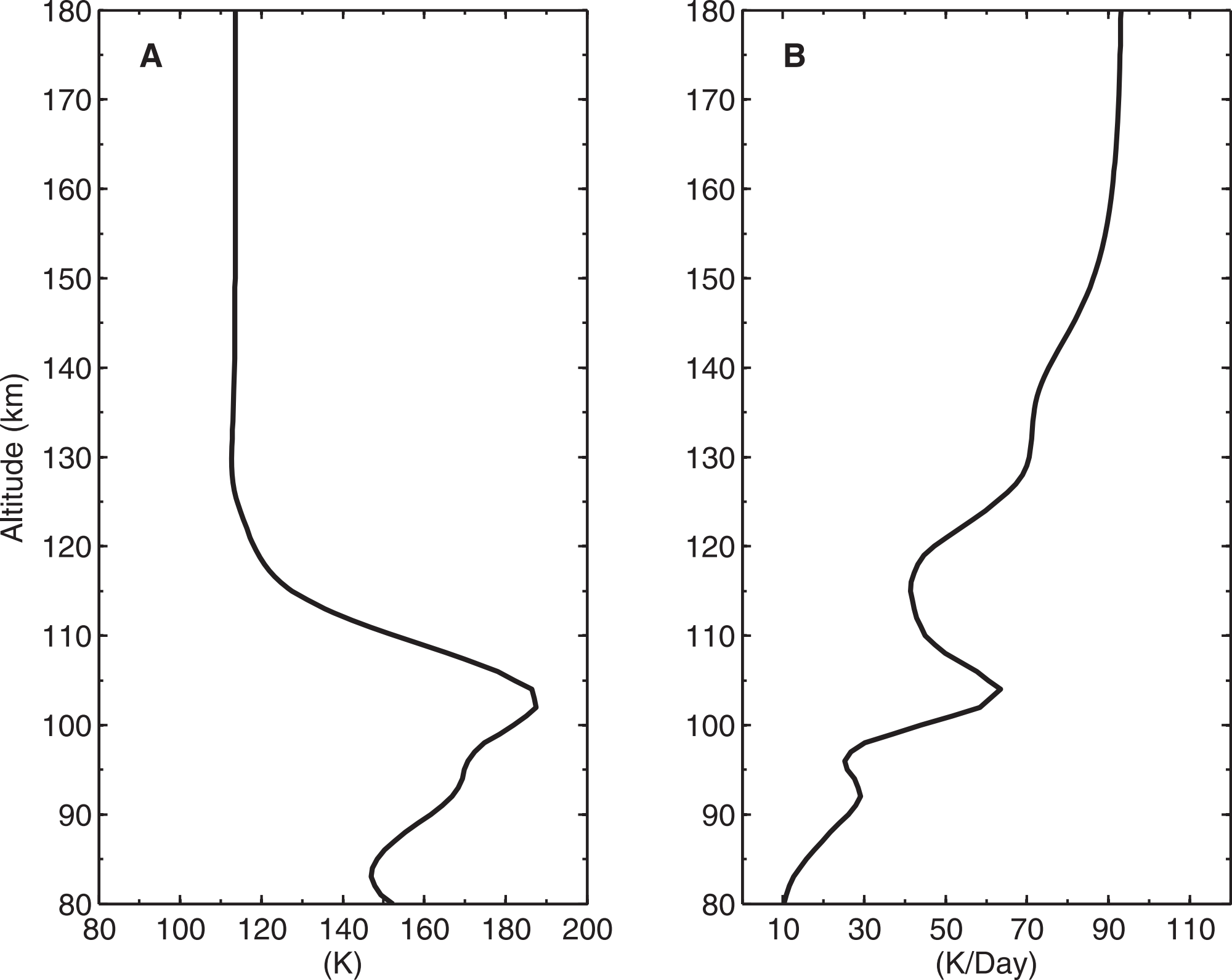
A
B
Altitude (km)
180
170
160
150
140
130
120
110
100
90
80
80
100
120
140
160
180
200
(K)
10
30
50
70
90
110
(K/Day)

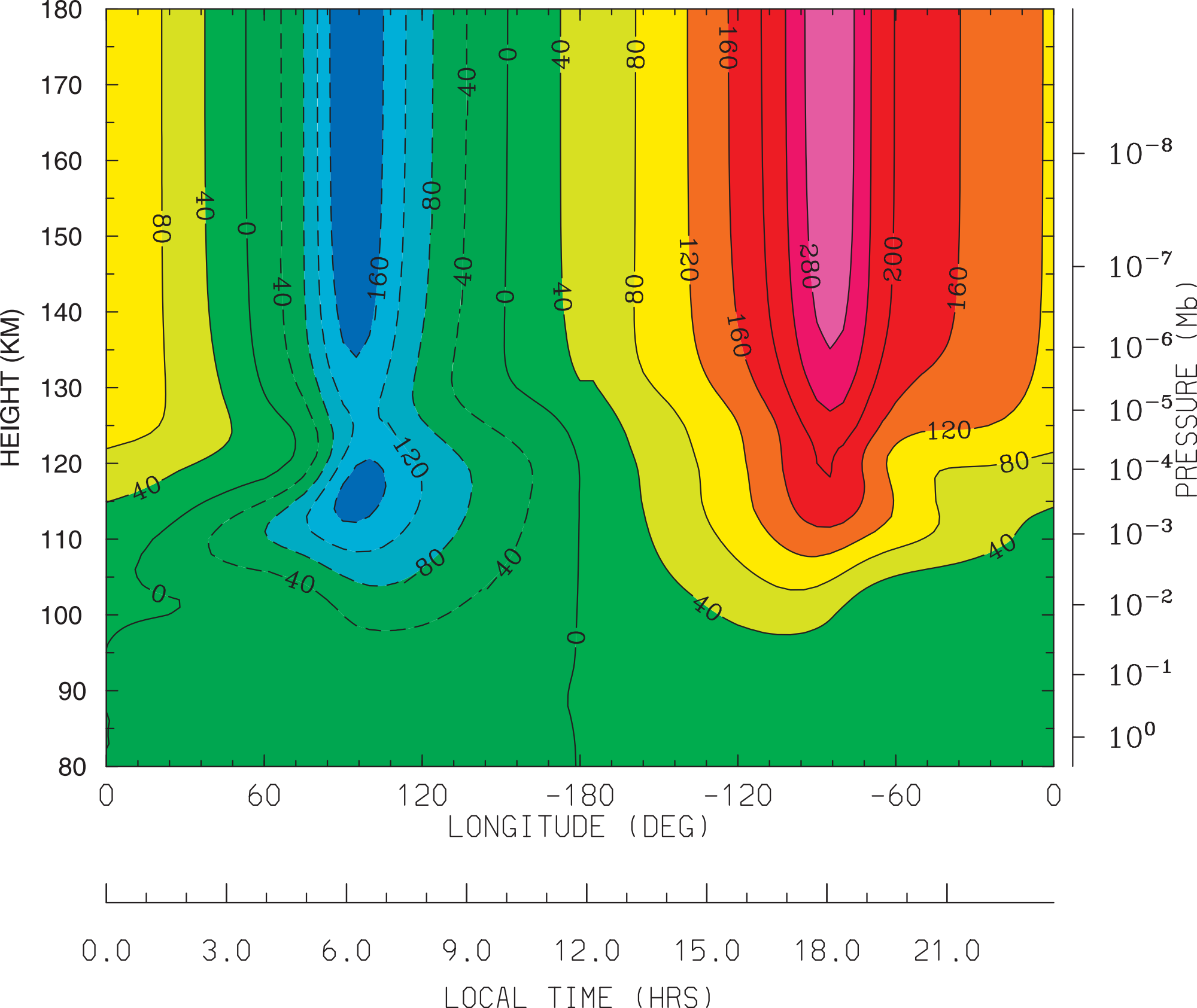
HEIGHT (KM)
180
170
160
150
140
130
120
110
100
90
80
PRESSURE (Mb)
10^{-8}
10^{-7}
10^{-6}
10^{-5}
10^{-4}
10^{-3}
10^{-2}
10^{-1}
10^{0}
0
60
120
-180
-120
-60
0
LONGITUDE (DEG)
0.0
3.0
6.0
9.0
12.0
15.0
18.0
21.0
LOCAL TIME (HRS)

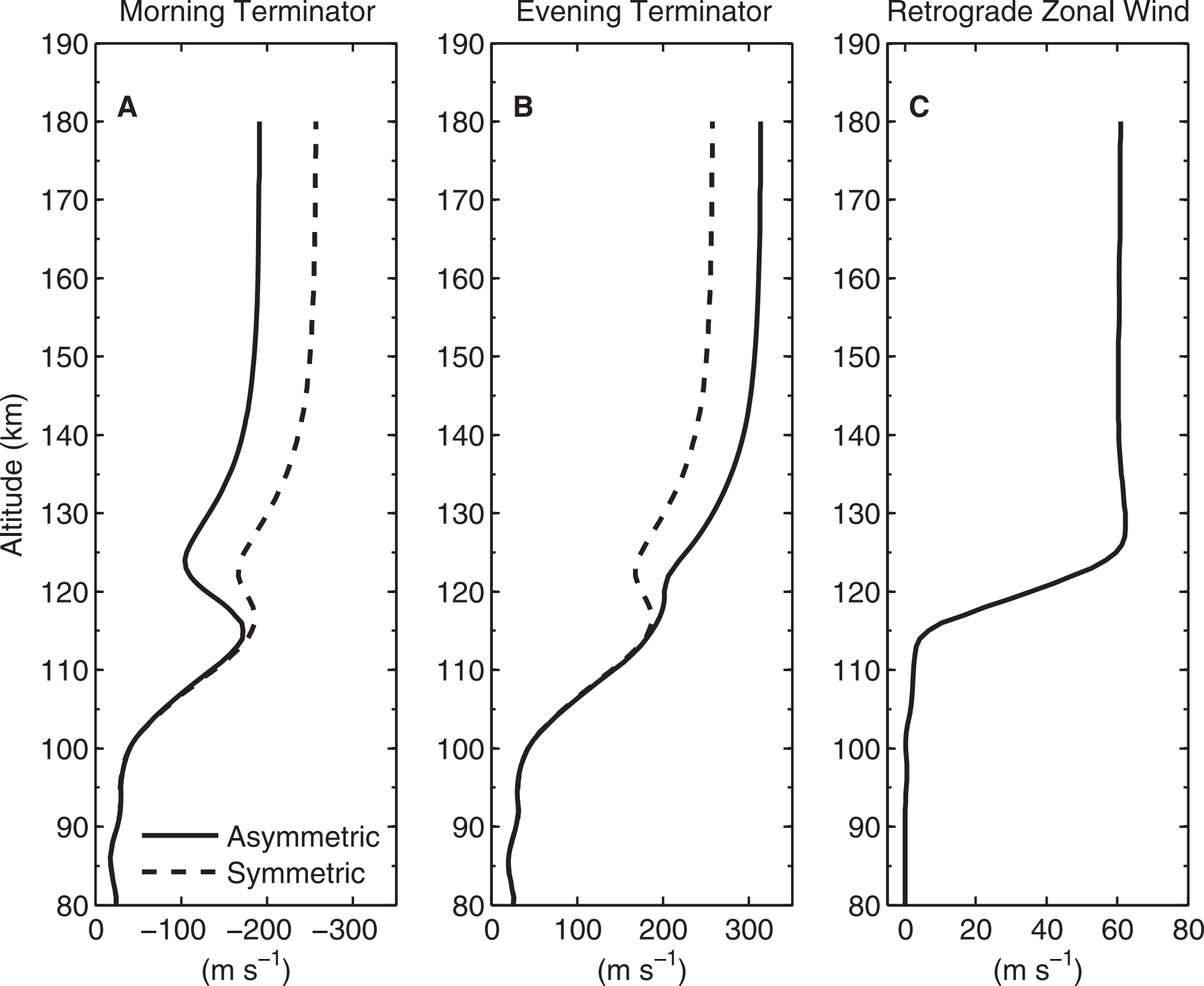
Morning Terminator
Evening Terminator
Retrograde Zonal Wind
A
B
C
Altitude (km)
190
180
170
160
150
140
130
120
110
100
90
80
0
−100
−200
−300
100
200
300
20
40
60
80
(m s^{-1})
Asymmetric
Symmetric

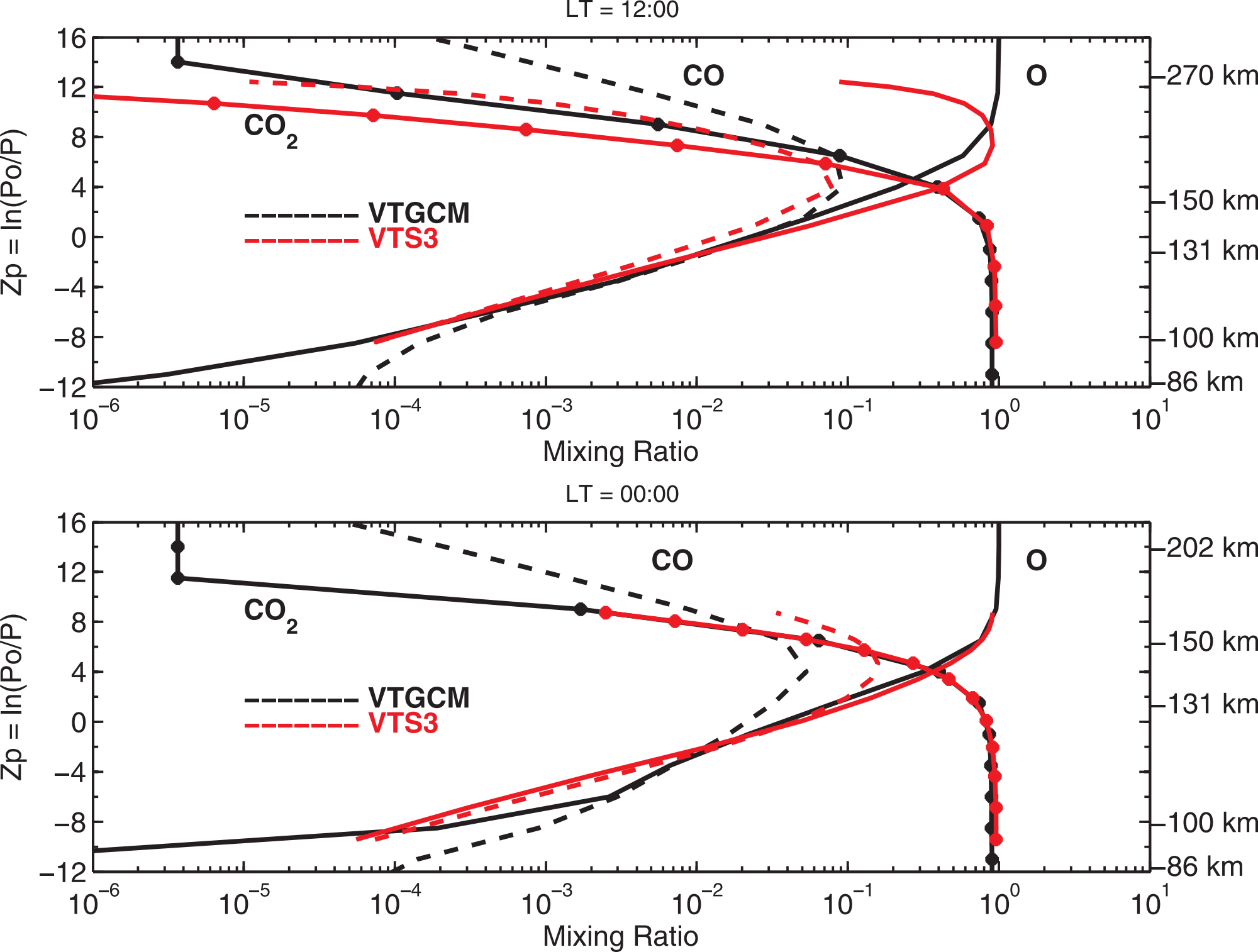
LT = 12:00
CO
O
CO2
VTGCM
VTS3
Zp = ln(Po/P)
Mixing Ratio
270 km
150 km
131 km
100 km
86 km
LT = 00:00
CO
O
CO2
VTGCM
VTS3
Zp = ln(Po/P)
Mixing Ratio
202 km
150 km
131 km
100 km
86 km

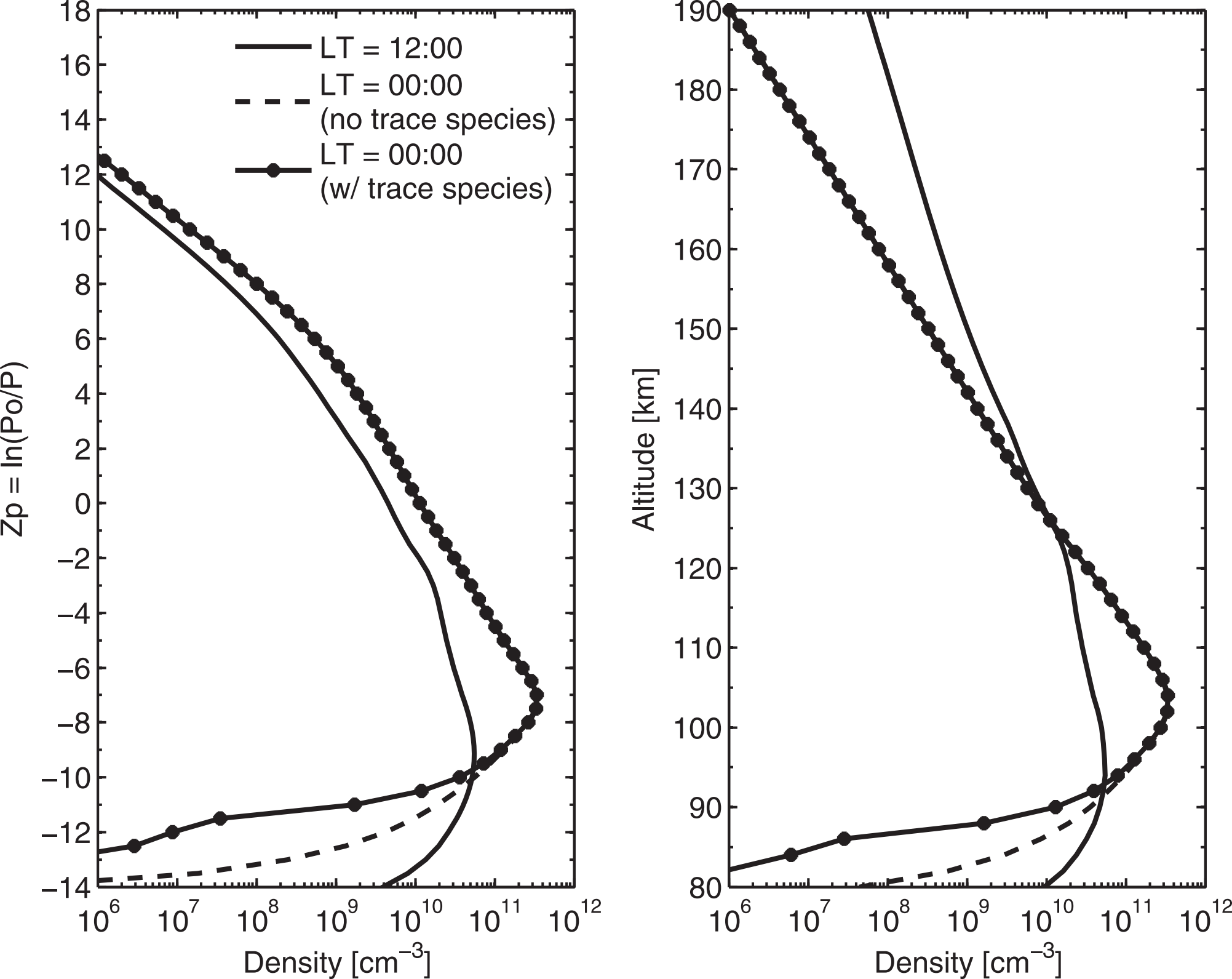
LT = 12:00
LT = 00:00
(no trace species)
LT = 00:00
(w/ trace species)
Zp = ln(Po/P)
Altitude [km]
Density [cm^{-3}]
Density [cm^{-3}]

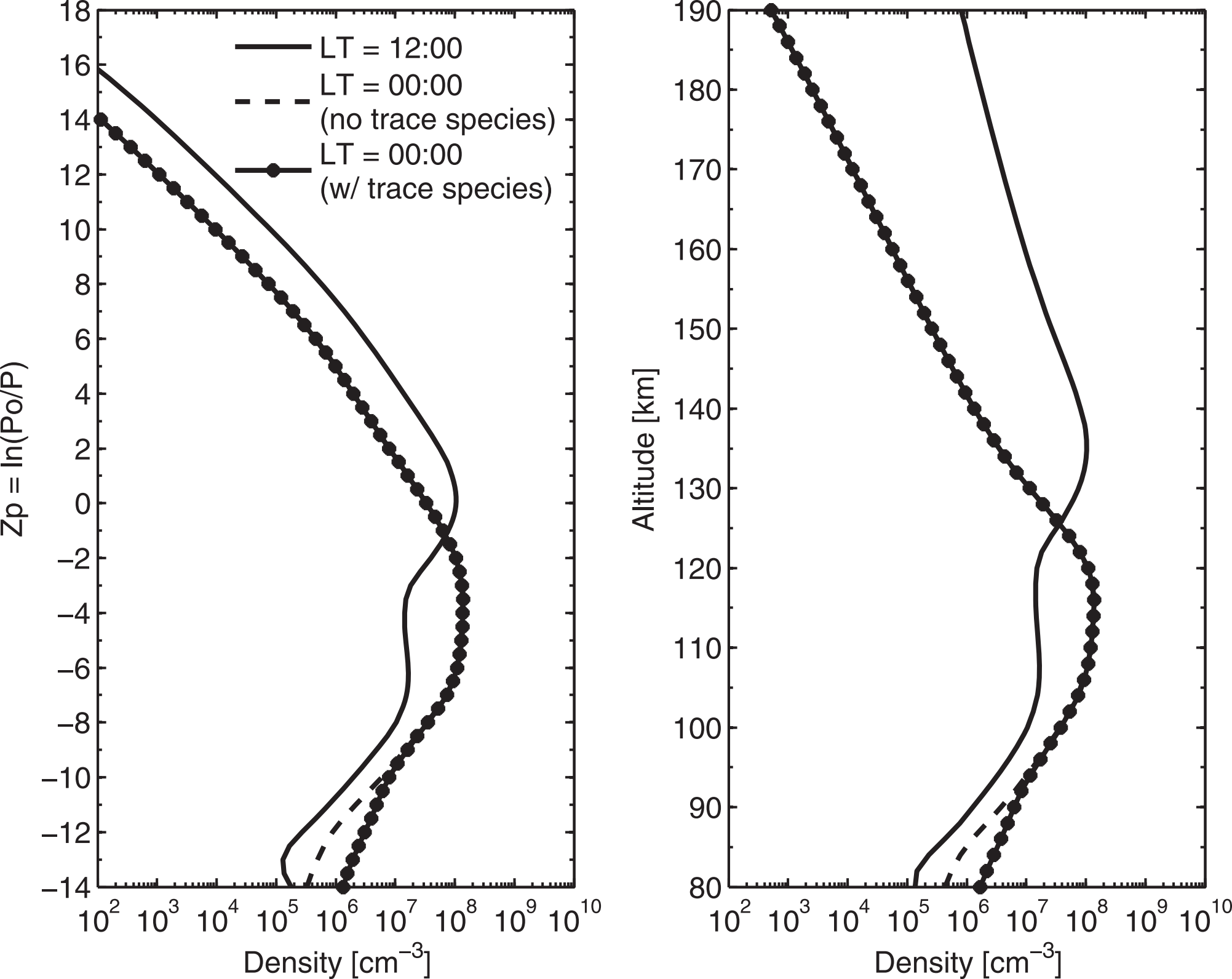
LT = 12:00
LT = 00:00
(no trace species)
LT = 00:00
(w/ trace species)
Zp = ln(Po/P)
Density [cm^{-3}]
Altitude [km]
Density [cm^{-3}]

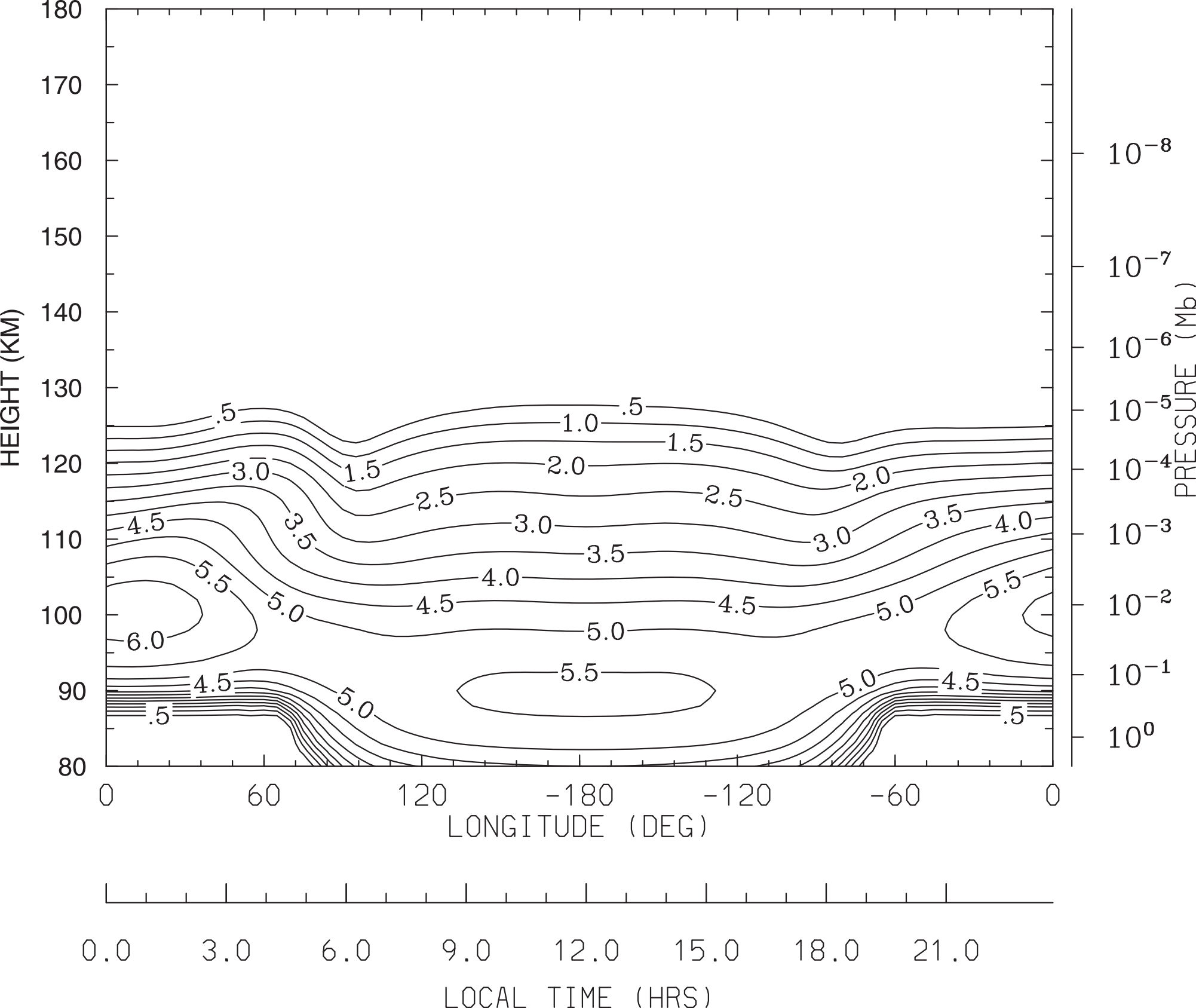
HEIGHT (KM)
180
170
160
150
140
130
120
110
100
90
80
PRESSURE (Mb)
10^{-8}
10^{-7}
10^{-6}
10^{-5}
10^{-4}
10^{-3}
10^{-2}
10^{-1}
10^{0}
.5
1.0
1.5
2.0
2.5
3.0
3.5
4.0
4.5
5.0
5.5
6.0
0
60
120
-180
-120
-60
0
LONGITUDE (DEG)
0.0
3.0
6.0
9.0
12.0
15.0
18.0
21.0
LOCAL TIME (HRS)

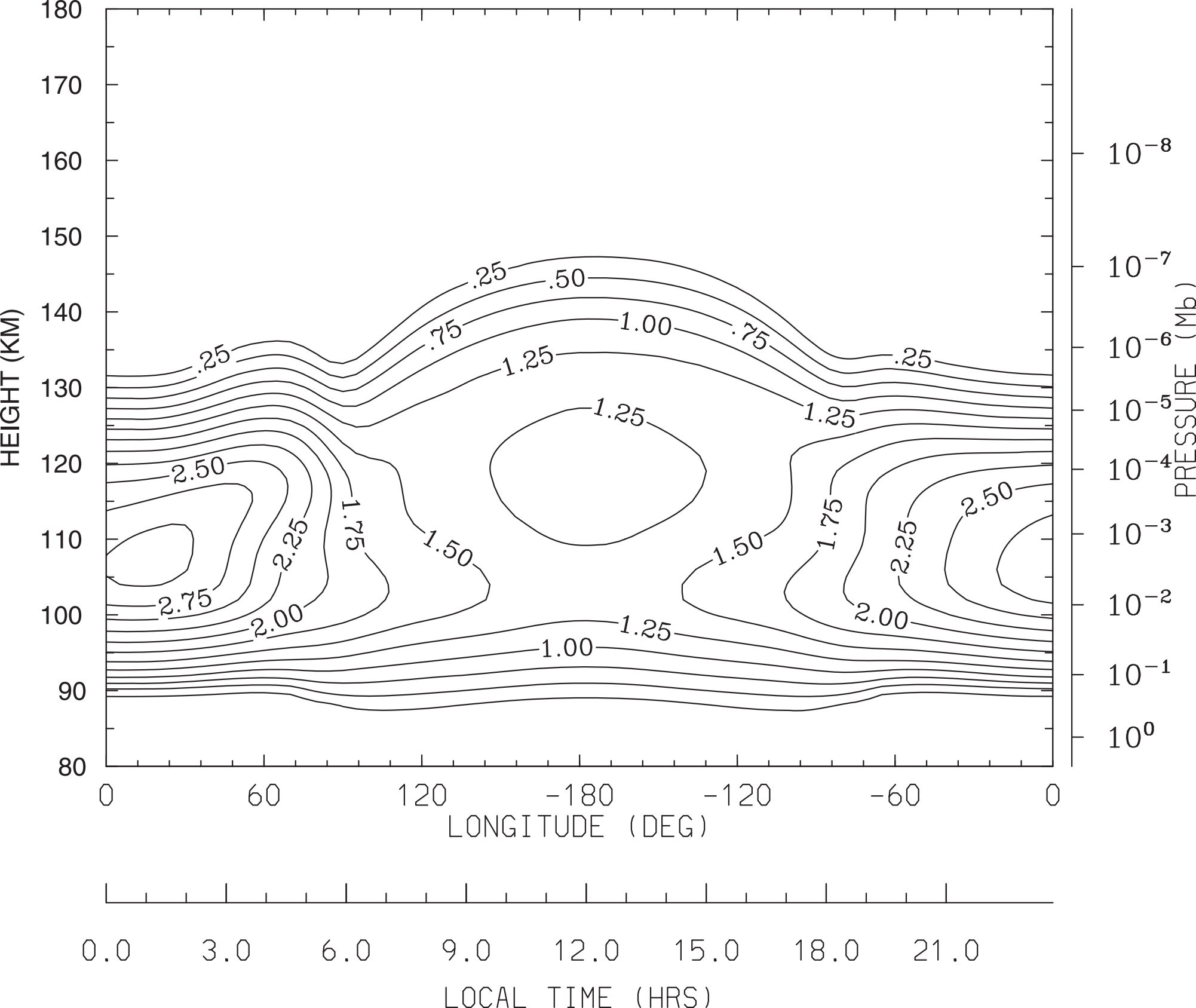
HEIGHT (KM)
180
170
160
150
140
130
120
110
100
90
80
PRESSURE (Mb)
10^{-8}
10^{-7}
10^{-6}
10^{-5}
10^{-4}
10^{-3}
10^{-2}
10^{-1}
10^{0}
.25
.50
.75
1.00
1.25
1.50
1.75
2.00
2.25
2.50
2.75
0
60
120
-180
-120
-60
0
LONGITUDE (DEG)
0.0
3.0
6.0
9.0
12.0
15.0
18.0
21.0
LOCAL TIME (HRS)

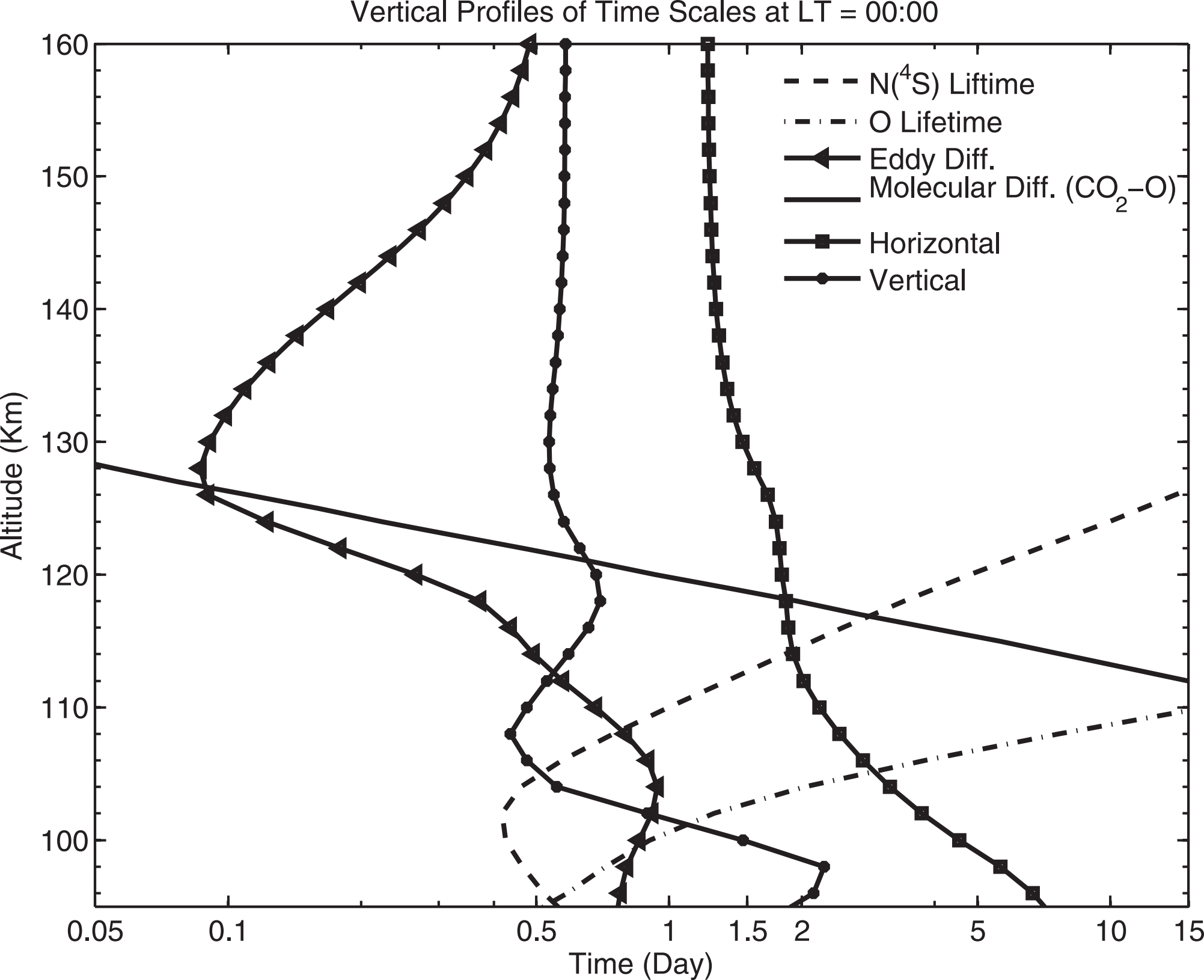
Vertical Profiles of Time Scales at LT = 00:00
160
150
140
130
120
110
100
Altitude (Km)
0.05
0.1
0.5
1
1.5
2
5
10
15
Time (Day)
N(4S) Liftime
O Lifetime
Eddy Diff.
Molecular Diff. (CO2–O)
Horizontal
Vertical

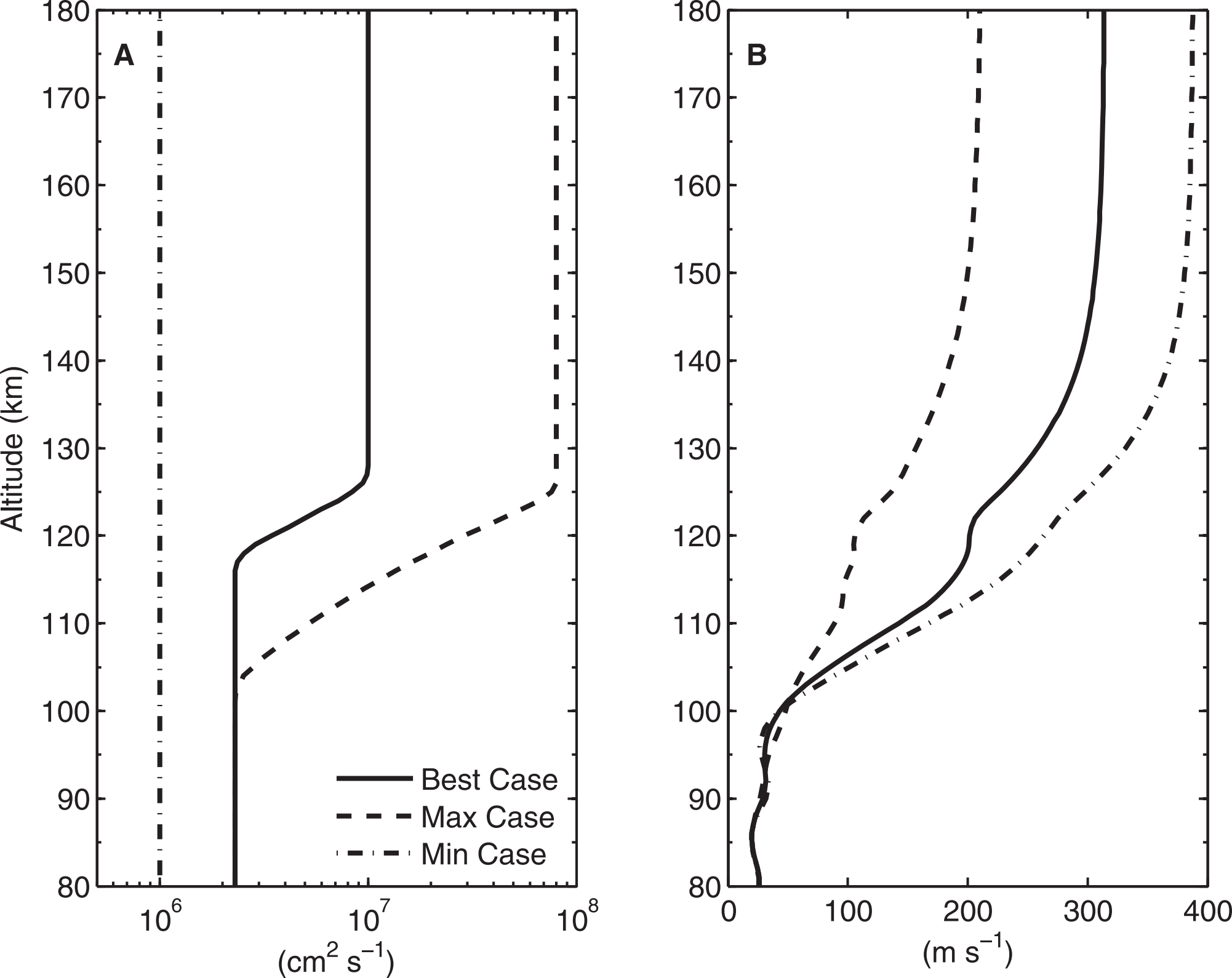
A
B
Altitude (km)
180
170
160
150
140
130
120
110
100
90
80
10^6
10^7
10^8
($cm^2\ s^{-1}$)
0
100
200
300
400
($m\ s^{-1}$)
Best Case
Max Case
Min Case